Shortening of the axial zone, pyrenees: Shortening sequence, upper crustal mylonites and crustal strength

Nicolas Bellahsen, Léa Bayet, Y. Denèle, M. Waldner, Laura Airaghi, Claudio Rosenberg, Benoît Dubacq, F. Mouthereau, M. Bernet, Raphaël Pik, et al.

Shortening of the Axial Zone, Pyrenees: shortening sequence, upper crustal mylonites and crustal strength

N. Bellahsen[1], L. Bayet[1], Y. Denele[2], M. Waldner[1], L. Airaghi[1], C. Rosenberg[1], B. Dubacq[1], F. Mouthereau[2], M. Bernet[4], R. Pik[3], A. Lahfid[5], A. Vacherat[1]

[1] Sorbonne Université, CNRS-INSU, Institut des Sciences de la Terre Paris, UMR 7193, F-75005, Paris, France

[2] Géosciences Environnement Toulouse, Université de Toulouse, CNRS, IRD, UPS, CNES, 31400 Toulouse, France

[3] CRPG, UMR 7358 CNRS-Université de Lorraine, BP20, 15 rue Notre-Dame des Pauvres, 54500 Vandoeuvre-lès-Nancy, France

[4] Université Grenoble Alpes, ISTerre, 38000 Grenoble, France.

[5] BRGM, 3 avenue Claude Guillemin, 45060 Orléans Cedex 2, France

Corresponding author: nicolas.bellahsen@sorbonne-universite.fr

Abstract

The strength of the lithosphere may be constrained qualitatively by field observations on localized vs distributed modes of deformation and by the mineral assemblages formed during deformation. The internal deformation of the Bielsa basement unit of the Pyrenean Axial zone is investigated through structural, microstructural and thermometric data. In this area, shortening is widely distributed as attested by the folded attitude of the interface between the basement and its sedimentary Triassic cover. Shortening is estimated around 1.7 km (13%) from a regional balanced cross-section and should be considered in pre-Pyrenean reconstructions. Shortening probably occurred before strain localization on crustal ramps as suggested by zircon fission-track analysis. Distributed shortening is characterized at small-scale by low-temperature mylonites and cataclasites. In thin-section, feldspar originally present in magmatic rocks is partially to totally sericitized. This transformation led to significant weakening of the rock and took place in the 250-350°C temperature range. Sericitization is ubiquitous, even in un-deformed granodiorites. This shows that the weakening effect of sericitization not only occurs in ultra-mylonites, ultra-cataclasites and

phyllonites but also more generally in the upper crust early during the shortening history, with implications for the shortening style. Estimates of the geothermal gradient suggest that inherited thermicity may also have influenced the style of shortening. We propose that the upper crust was very weak before or at the onset of its shortening due to high-thermal gradient and fluid circulation that induced large-scale sericitization in greenschist facies conditions. This has strong implications on the rheological evolution of the upper crust submitted to metamorphic alteration in the greenschist facies and below.

Keywords: collision, rheology, Pyrenees, basement, greenschist

1. Introduction

The strength of the continental crust is usually estimated by extrapolating flow laws derived from laboratory experiments on quartz (Brace and Kohlstedt, 1980) extrapolated to large scales of space and time. This approach coupled with Byerlee's law (Byerlee, 1978) provides a "simple" two-layer rheological profile including a brittle upper- and a ductile lower part (Ranalli and Murphy, 1987), although it can be more complex. This model is consistent with field observations, showing that deformation is rather localized in fault zones with cataclastic rocks in the upper crust and more distributed in shear zones with mylonites in the lower crust (e.g., Scholz, 1989), and with a transitional regime at the brittle-ductile boundary (e.g., Handy et al. 2007; and references therein). Quartz being the most abundant mineral in the crust, its mechanical behavior is generally used to model the strength of the ductile crust. However, if interconnected layers (Handy, 1994) of weaker phases are present, the mechanical behavior of the polymineralic crustal rocks is dramatically altered. These weak phases often comprise phyllosilicates (e.g., Janecke and Evans, 1988; Shea and Kronenberg, 1993; Wintsch et al., 1995; Gueydan et al., 2003).

Sericitization, i.e. the breakdown of feldspar into much smaller-sized mica (e.g., Wintsch et al., 1995), is a common process during crustal deformation under greenschist facies conditions (e.g. Wibberley, 1999). It is generally accompanied by crystallization of kaolinite, chlorite, phrenite, pumpellyite, calcite and albite, by-products of the hydrothermal alteration of granitoids (e.g., Ciesielczuk and Janeczek 2004). Sericitization of feldspars triggers both an increase of the rock ductility and a decrease of its strength. The deformation of mica-rich

64 rocks (such as phyllonites) often results in penetrative schistosity, and S/C-C' type fabrics
65 (e.g., Jefferies et al., 2006). The strength of such rocks is significantly lower than that of
66 quartzo-feldspatic rocks (e.g. Wintsch et al., 1995) and experiments on anisotropic rocks have
67 shown that even a small amount of phyllosilicates (e.g., talc, Collettini et al., 2009a;
68 Niemeijer and Spiers, 2005; Niemeijer et al., 2010) has a large effect on bulk rock strength.
69 Phyllosilicate fabric in fault zones may therefore explain the weakness of some crustal faults,
70 such as the San Andreas fault (Lachenbruch and Sass, 1980; Zoback et al., 1987; Holdsworth
71 et al., 2011; Carpenter et al., 2011), the Zuccale Fault (Collettini et al., 2009b), and the
72 Median Tectonic Line (Jefferies et al., 2006).

73 The initiation of syn-kinematic phyllonitization increases the contrast between the strength
74 of the fault zone and the strength of the adjacent rocks, enhancing strain localization. Less
75 studied is the case where pre-kinematic rock alteration may decrease the rock strength. Such
76 case can be found in context where distributed deformation is observed. However, distributed
77 deformation of upper crustal basement rocks is generally poorly studied (except in e.g., Butler
78 et al., 2002; Butler and Mazzoli, 2006; Carminati, 2009, Mazzoli et al., 2009) mainly because
79 markers are usually lacking and polyphased tectonic history complicates strain analysis. In the
80 basement units of the Axial Zone in the Pyrenees (**Fig. 1**), such a study is possible thanks to
81 late Variscan granitoids, that appear to be low-deformed at solid state during late Variscan
82 times that bear Alpine deformation. Moreover, the Triassic cover crops out in many places
83 above the basement in the Axial Zone. This provides a marker to investigate the Alpine
84 shortening in terms of localization and magnitude, and to study the related deformation
85 mechanisms of crustal rocks at temperature around and below 300°C. Indeed, in the Axial
86 Zone, basement units are usually considered to have been buried and deformed during
87 Tertiary below 300°C (e.g., Fitzgerald et al., 1999; Sinclair et al., 2005; Jolivet et al. 2007;
88 Gibson et al., 2007; Metcalf et al., 2009). Shortening is accompanied by metamorphism in
89 greenschist facies conditions that affected both the Paleozoic sedimentary and
90 metasedimentary rocks and the late-Variscan granites and granodiorites.

91 The present contribution first reports on the structural evolution of the Axial Zone basement
92 units. For this purpose, we present a structural study consisting of a regional, balanced cross-
93 section and an outcrop-scale analysis of the shortening kinematics. Second, this contribution
94 documents the microstructural evolution of basement rocks and the weakening processes that
95 they undergo before and during deformation. A thermometric and thermochronological study
96 was carried out to document the thermal and metamorphic history. Eventually, the effects of

widespread sericitization of the granite/granodiorite and of the inherited hot geothermal gradient and their implications on crustal rheology are discussed.

2. Geological setting

The Pyrenean mountain belt results from the closure of a rifted domain located in the present-day North Pyrenean Zone (NPZ, **Fig.1**). This rift opened during Albo-Cenomanian times at the eastern end of the Bay of Biscay (Puigdefabregas and Souquet, 1986) and was subsequently shortened during upper Cretaceous (around 84 Ma) to Oligocene times (Olivet, 1996). During the collision, north-verging crustal thrusts deformed the NPZ, while south-verging ones affected the Axial Zone and the South Pyrenean Zone (SPZ, **Fig. 1, 2**). While in most of the SPZ, the structural style is thin-skinned, the Axial Zone is composed of few basement units, namely the Lakora, Gavarnie, Bielsa-Millares, and Guarga in the western part (**Fig. 2**) and Gavarnie/Nogueres, Orri, and Rialp in the East (Teixell, 1996; Munoz, 1992; Roure et al., 1989; Mouthereau et al., 2014). The nappe stack is usually described as an antiformal stack, where the lowest unit is the youngest. This antiformal stack geometry is indeed clear in the western axial zone (Jolivet et al. 2007; Teixell, 1998; Teixell et al., 2018) but was questioned in the central axial zone (Cochelin et al., 2018) contrarily to what was classically proposed (Munoz, 1992; Beaumont et al., 2000; Roure et al., 1989). As this study focuses on the western part, this controversy will not be discussed in the contribution.

In the westernmost part of the axial zone (Teixell, 1996), the Lakora thrust (**Fig. 1, 2**) emplaced the Iguntze massif over the Gavarnie unit during at least Lutetian times (Teixell, 1996) during the deposition of the Hecho group turbidite series (Labaume et al., 1985) in the Jaca foreland basin. In the footwall of the Lakora thrust, the Larra thrust affected the Mesozoic cover of the Gavarnie unit and, later on, the Gavarnie thrust affected the basement, triggering the southward migration of the foreland basin during late Eocene-early Oligocene. During Oligocene times, the Guarga unit was emplaced below the turbiditic basin and controlled its southward migration and evolution into a molasse-type overfilled basin (**Fig. 2**).

Further east, the Lakora unit is ill-defined, especially its southern boundary. The Gavarnie/Lakora unit, at the longitude of our study, is affected by a distributed zone of deformation including the Pic du Midi thrust, the Eaux Chaudes shear zones (Lamouroux et al., 1979; Henderson and McCaig, 1996; Ingles et al., 1999), and the Pic Long thrust, from

North to South, respectively (see Jolivet et al., 2007). This large zone is probably the eastward continuation of the Lakora thrust (**Fig. 2**).

In the southern part of this diffuse zone of deformation, the Lakora/Gavarnie unit is composed of the Late Variscan Neouvielle granitic massif and surrounding Paleozoic rocks (Gleizes et al., 2001; Roman-Berdiel et al., 2004) and emplaced above the Gavarnie thrust. In the Neouvielle massif, alpine reverse shear zones linked to the Eaux Chaudes thrust system were dated at about 47 +/- 8 Ma or 48 +/- 2 Ma (Wayne and McCaig, 1988). These ages are similar to the probable age of reactivation of the Merens shear zone activity further East around 50 Ma (McCaig and Miller, 1986). It should be noted that the formation of the numerous shear zone of the Pyrenees lead to several discussions about the age of their formation, variscan or alpine. Although some authors have proposed that some of these shear zone belonging to a variscan anastomosed network that have influenced the evolution of the variscan gneiss dome systems (Denèle et al., 2007; Cochelin et al., 2017) and the dynamic of pluton emplacement (Gleizes et al., 1998; Denèle et al., 2008), they consider also that these shear zone have been clearly reactivated during alpine orogenesis as in the Neouvielle pluton (Gleizes et al., 2001) and the Merens zone (Denèle et al., 2008) that could explain alpine ages of synkinematic phyllosilicates (see above). Apatite Fission-Tracks (AFT) in Neouvielle ages range between 22 and 27 Ma while in northern massif (Bordères Louron) the ages range between 31 and 36 Ma (Morris et al., 1998; Jolivet et al., 2007).

In the footwall of the Gavarnie thrust, the Bielsa/Millares unit is composed of the Late Variscan Bielsa granitic massif and surrounding Paleozoic rocks (**Fig. 3**). This unit can be subdivided into two sub-units: the Millares and the Bielsa unit. A basement thrust is probably present below the Bielsa unit (Casas et al., 2003; Jolivet et al., 2007) although it does not crop out. Before this thrust initiation (Miocene, Jolivet et al., 2007), the Bielsa/Millares unit was part of a larger basement unit, namely the Guarga unit (**Fig. 2**) (Teixell, 1996), which emplacement tilted the Lutetian Hecho turbidites in the Jaca basin (Labaume et al., 1985; Teixell, 1996) probably during Late Oligocene times (Jolivet et al., 2003). In the Bielsa granite, AFT ages range between 10 and 20 Ma (Morris et al., 1998; Jolivet et al., 2007) and have been interpreted as witnessing the out-of-sequence initiation of the Bielsa thrust (Jolivet et al., 2007), i.e. after the Guarga thrust initiation.

South of the Bielsa unit, the Monte Perdido unit is a sedimentary nappe that might root in the Eaux Chaudes shear zones (Labaume et al., 1985; Teixell, 1996).

In the central Axial Zone, further East, in the Gavarnie unit, a zircon fission-track (ZFT) age of 49 Ma was provided by Sinclair et al. (2005). AFT ages range between 26 to 45 Ma (Fitzgerald et al., 1999; Sinclair et al., 2005), whereas apatite (U-Th)/He ages are between 17 and 37 Ma (Gibson et al., 2007).

In the Orri unit, structurally below the Gavarnie unit, AFT ages in the Maladeta massif range between 17 and 35 Ma (Morris et al., 1998; Fitzgerald et al., 1999; Sinclair et al., 2005; Gibson et al., 2007), apatite (U-Th)/He ages range between 10 and 35 Ma (Gibson et al., 2007). ZFT data present both Mesozoic (104 and 159 Ma) and Cenozoic ages (49 Ma), (Sinclair et al., 2005). These ages show a rapid exhumation during early Oligocene times, following and followed by a slower exhumation during Eocene and late Oligocene times (Fitzgerald et al., 1999).

3. Structural and microstructural results

3.1. Regional cross-section and structural study

As shown by the cross-section (**Fig. 3, 4**), the lower Triassic layers are still attached to the basement top and both are folded. There are up to about 9 antiforms; their wavelength is about 1 km. Six steep faults are associated to some of these antiforms (**Figs. 3, 4**) and the synforms are marked by outcrops of Triassic layers (**Fig. 5, 6**). These layers are offset by steep faults, located on the southern side of the synforms. The faults are either normal or reverse: the southernmost and the northern most ones appear to be normal faults, while the other ones are reverse faults. The synforms are usually asymmetrical generally with steeper limbs on the faulted side (**Figs. 5, 6, 7b,c**).

The cross-section has been restored considering that the basement top (i.e. the lower Triassic layers) has a constant length during shortening. The Triassic layers were probably deformed during shortening (e.g., lengthening of the layers), by a probably very low amount, which is negligible for restoration purposes. The second main assumption concerns the geometry of the sub-vertical faults. Here, we chose to restore these faults (**Fig. 4**) as we consider them to be pre-orogenic for the following reason: the Fobillons and Punta Suelza klippes are clearly not as folded as the underlying Triassic layers and basement top (**Figs. 4 and 7a**). This means that

folding and the vertical faults predated the end of the burial of Bielsa unit below Millares and Gavarnie. If the vertical faults were coeval with the Bielsa thrust, the Millares thrust would have been folded too, but this is not the case. Assuming this, the restoration provides an amount of shortening of 1.7 km (13%). If the sub-vertical faults were syn-shortening, the amount of shortening would have been slightly higher. The faults may be Cretaceous in age (either pre- or syn-Cenomanian) as suggested by Johnson et al. (1996).

The northernmost synform (**Fig. 3, 4, 5**, Urdiceto synform) varies structurally along strike. East of the Lago Urdiceto, the synform is pinched and associated to significant deformation in the basement (**Fig. 6a**), as shown by a penetrative schistosity (**Fig. 6, 8a**), with some shear zones (**Fig. 6, 9**). This schistosity is especially well expressed where the basement shows a thick altered/weathered upper horizon (several tens of meters; **Fig. 8**). The basement weathering seems to predate the shortening as unaltered areas present a less penetrative schistosity (**Fig. 8b**). This weathering is most likely Permian in age as the Triassic cover is not affected. West of the Lago Urdiceto, shortening was less intense and the basement presents less deformation (**Fig. 5, 6**).

Within this synform, several features attest for shortening in the cover. Top-to-the-South kinematic indicators are observed above the basement-cover interface on the northern side of the synforms (**Fig. 5, site 37/38; Fig. 10a**): there, no large-scale décollement occurred but the schistosity is deflected in a sigmoidal pattern due to shearing along the bedding planes. Further up in the cover, tight folds are accompanied by coeval sub-vertical schistosity (**Figs. 10b, c**) along with a vertical stretching attested by numerous sub-horizontal veins (**Fig. 10b**) with sub-vertical fibrous crystals of calcite, quartz, and chlorite. These cover folds with wavelength much smaller than those of the basement top implies that there is a slight décollement above the basement top unconformity.

Within the synform further south (**Figs. 3, 4**), the border fault dips south and is reverse (**Figs. 4, 6, 7c**). Folds are associated with a steep cleavage (**Fig. 7c**) and the cover is affected by reverse faults, at shallower dip than the main border fault (**Fig. 11**).

Between the synforms, shear zones are widespread in the basement. They consist of thin (< 1 m) zones dipping 45 to 70° N with both south- and north-verging kinematics (mainly south-verging, **Fig. 6, 9**). Quartz crystals are affected by cataclastic deformation within shear zones, while chlorites are affected by a more ductile-like deformation and present sigmoidal shapes

(**Fig. 12 and 13**). Alpine schistosity and shear zones are also characterized by interconnected layers of white micas (see below).

The steep faults (**Fig. 5, 6, 7b, c, 11a**) bordering the synforms have been sampled and show typical cataclastic textures (**Fig. 12a, b**). The quartz are broken up in millimetric clasts. These structures are linear and affect a hydrated protolith: phases such as chlorites and white micas (in feldspars, see below) are widespread in thin sections but do not affect significantly the distribution of cataclasites (**Fig. 12a, b**). The cataclasites do not either seem to control the distribution of the hydrated phases.

3.2. Sericitization

In samples of un-deformed rocks (**Fig. 13a, 14a**), the mineral assemblage is composed of quartz, K feldspars, plagioclase, chlorites, biotites, white micas as well as accessory minerals such as alanites, zircons, titanites, rutiles, pyrites, apatites. Quartz and feldspars form subhedral to anhedral millimetric grains (**Fig. 12**). Quartz commonly contains fluid inclusion planes. Chlorites are large (few tens of mm) and they overgrow biotites, with titanites and rutiles inclusions. The chlorites are also found smaller interlayered with white micas.

In undeformed and weakly deformed samples, K feldpsar is replaced by albite that grows in fractures and along mineral cleavage (**Fig. 14a**), where white micas and carbonates are also observed. With increasing destabilization, in more deformed samples, both albite and white micas develop in these K feldpars (**Fig. 14b**) and totally replace them (**Fig. 14d, e**). Locally, prehnites and epidotes can be observed. Moreover, white micas are also associated to chlorites that derive from the biotite destabilization (**Fig. 14c**).

In samples from deformed rocks, the amount of albite and white mica increases and a schistosity appears, formed by the alignment of micas and chlorites (**Fig. 14d**). The rock mainly consists of quartz, white mica, and albite. Quartz is mainly affected by undulose extinction and some fractures, but only little or no dynamic recrystallization (**Fig. 13b**).

In very deformed rocks, the assemblage is mainly composed of deformed quartz and white micas (**Fig. 14e**). Thus, the amount of white micas has increased with deformation. This is most likely due to the total sericitization of feldpars that is probably favored by mineral fracturing, hence fluid infiltration. White micas are often aligned and define micro-shear

zones and schistosity (**Fig. 13c**). Quartz clasts and chlorites are embedded in a white mica "matrix" (**Fig. 13c, 14e**), with some calcite close to faults affecting the basement (that may have provided fluids with calcium). In the white mica "matrix", very small scale aggregates of poorly oriented grains can be observed (**Fig. 14e**).

4. Geo-thermometry

Phyllosilicates provide thermobarometry constraints on samples from the Bielsa massif (**Fig. 15**). Thermodynamic modelling using multi-equilibrium thermobarometry yields crystallization temperatures in the range 250-300°C for micas (Dubacq et al., 2010) and chlorites (Vidal et al., 2006) (both +/- ~50°C).

The Raman Spectrometry of Carbonaceous Material (RSCM) method (Beyssac et al., 2002; Lahfid et al., 2010) is based on the quantitative study of the degree of (irreversible) graphitization of carbonaceous material (CM), which provides the maximal temperature (Tmax) attained during the rock history. Tmax can be determined in the range 200–650°C (Beyssac et al., 2002; Lahfid et al., 2010), with absolute precisions of ca. 50°C between 650 and 300°C and ca. 25°C between 330 and 200°C. Relative uncertainties between samples are probably much smaller (around 10-15°C according to Beyssac et al., 2004, 2007; Gabalda et al., 2009; Vitale Brovarone et al., 2013). Raman spectra (Supplementary Material) were measured and analyzed following Beyssac et al. (2002, 2004, 2007) and Lahfid et al. (2010). Raman spectra were obtained using a Renishaw InVIAReflex microspectrometer (BRGM, Orléans, France) with a 514-nm argon laser on polished thin sections from CM-rich Mesozoic limestones (Cenomanian, see **Fig. 3** for location).

The RSCM study yields Tmax between 236 and 264 °C +/- 30°C for the cover of the Bielsa massif (**Table 1**). The samples are part of the Bielsa unit, from the Cenomanian cover, mostly from the southern part of the area. There, the cover is slightly detached from the basement and the Triassic layers. However, Tmax obtained from these samples may be confidently assigned to the Bielsa unit. In the Gavarnie unit, one RSCM analysis indicates Tmax of 328°C +/- 30°C (**Table 1, Fig. 16** for location).

5. Zircon fission-track data and thermal history

281

282 5.1. Zircon fission track data

283 In the Neouvielle massif, ZFT ages were obtained from three samples, NAZ-1, NAZ-7 and
284 NAZ-6, collected along an elevation profile at 1881 m, 2400 m, and 2700 m, respectively
285 (**Table 2, Fig. 16**). No major faults were mapped between these samples, although some shear
286 zones are present (Fig. 17). These shear zones do not present very high displacement and
287 were dated to be active around 48 Ma (Ingles et al., 1999; Wayne and Mc Caig, 1998). All
288 three samples pass the χ^2-test and have central ages at around 45-46 Ma (**Fig. 16, Table 1**).
289 Nonetheless, the dispersion of single grains ages shows an interesting trend, decreasing from
290 16% at 1881 m elevation to 0% at 2700 m elevation. Furthermore. minimum ages, which
291 indicate the youngest coherent age population in a grain age distribution (Galbraith and
292 Laslett, 1993), are 38 Ma, 41 Ma and 45 Ma for samples NAZ-1, NAZ-7 and NAZ-6
293 respectively (**Fig. 16, Table 2**). In the Bielsa massif, 2 ZFT ages were obtained, with central
294 ages of 143 and 161 Ma, for elevations of 1680 and 2700 m, respectively (**Fig. 16, Table 1**).
295 Between these two samples no major faults were mapped (**Fig. 3, 16**)

296

297 5.2. Interpretation of ZFT data

298 The dataset from the Neouvielle massif provides Cretaceous to Cenozoic apparent cooling
299 ages (**Fig. 16**). The difference between the minimum ages and central ages of samples NAZ-1
300 and NAZ-7 may be related to slightly different closure temperatures in zircons that have
301 accumulated higher amounts of radiation damage because of high U concentrations. At least
302 the age and U concentration information shown in the radial plots display a weak trend of
303 higher U concentration grains having younger apparent cooling ages. The interpretation could
304 be the following: Cenozoic cooling started at around 46 Ma given the very similar central
305 ages of all three samples, but the increasing age dispersion and trend to younger minimum
306 ages for the lower elevation samples indicate that these rocks may have been affected by very
307 minor partial annealing, possibly resetting in the upper part of ZFT the partial annealing zone
308 for a short time before cooling to temperatures below the partial annealing zone.

309

310 5.3. Neouvielle thermal history

311 The thermal history for the Neouvielle massif (Gavarnie unit) is defined as follows. During
312 Mesozoic times, the temperature probably slightly increased due to rifting (the amplitude of
313 the temperature increase being difficult to constrain, see discussion below on the inherited
314 thermal structure) around 100 Ma and due to upper Cretaceous sedimentation. During Eocene
315 times, the temperature increased as a consequence of both the turbiditic basin formation
316 (Hecho group) and the overthrusting of the Lakora unit. The latter effect was probably limited
317 given the small amount of displacement on this thrust (see cross sections in Teixell, 1996).

318 The RSCM data are too scarce to be conclusive, but they provide a Tmax estimate of about
319 330°C (**Table 1**), also consistent with Jolivet et al. (2007), who estimated T of about 300°C
320 for the Neouvielle massif, mainly obtained from geochronological data. Thus, we set the
321 thermal peak of this unit to about 300°C reached before 50 Ma, given the ZFT central ages
322 around 46 Ma. From the rather limited ZFT data set that we have for the Neouville massif, it
323 seems that cooling started during mid-Eocene cooling. AFT ages for the Neouville massif
324 (Jolivet et al., 2005) indicate that cooling continued during Oligocene times (Fig. 18). Recent
325 U-Th/He data on zircons (Pik et al., in prep) will further constrain the Oligo-Miocene thermal
326 history. The cooling so far is constrained by AFT data from Jolivet et al. (2007) and their
327 thermal path and the age of activity of the Gavarnie thrust (**Fig. 17**)

328

329 5.4. Bielsa thermal history

330 The Jurassic ZFT ages obtained for the Bielsa massif (**Fig. 16**) indicated a different history.
331 Either the ages indicate a thermal event during Jurassic times or there has been a partial reset
332 during the mid-Cretaceous times (rifting). However, the grain age distribution does not
333 support the latter interpretation (they pass the χ^2-test and have 0% age dispersion). Due to the
334 limited number of samples and number of grains per samples, we cannot conclude about the
335 Mesozoic thermal history. However, it indicates that the Pyrenean shortening was not
336 responsible for any reset of this samples. It suggests a lower burial and/or a lower geothermal
337 gradient than, for the Neouvielle massif.

338 On **Fig. 17**, the Bielsa thermal path is colder than in the Neouvielle Massif as, in the Bielsa
339 massif, the analyzed samples are from a structural level slightly higher than the Neouvielle
340 massif. In the former samples are from the basement top, while in the latter there were
341 probably few km of basement above the samples. During Eocene times, heating of the Bielsa

massif is probably due to foreland sedimentation (Hecho group, **Fig. 17**) and possibly by the emplacement of the Gavarnie unit.

The Tmax of about 250°C according to the RSCM data (possibly Cenozoic in age) is in line with the Mesozoic ages ZFT we obtained: such temperature did not imply a Cenozoic reset of ZFT ages. We cannot derive from our data a complete thermal history but the exhumation during the last 35 Ma may be similar to the exhumation of the Neouvielle unit. The final thermal path is constrained from Jolivet et al. (2007) and the age of activity of the Guarga (**Fig. 2**) thrust that might have exhumed the Bielsa unit (**Fig. 17**).

6. Discussion

Our study shows that the small amount of shortening in the Bielsa unit is distributed at kilometer scale, as attested by the "basement antiforms" mapped in the field and shown in **Figures 6 and 7**. This distributed mode of shortening is also observed in the distributed ductile strain within both cover and basement units, where it may be explained by a pre-kinematic sericitization of the granitic basement.

6.1. Shortening kinematics and restoration

In our structural study, we restored the cross-section to its pre-orogenic stage, including the present-day steep faults, inferred to predate the shortening. Casas et al. (2003) proposed that these steep faults where rather late during the shortening history. Their main argument is that these faults do not seem to be overprinted by the contractional deformation. Indeed, the small-scale, low-angle reverse shear zone or faults do not crosscut the steep faults (**Fig. 11**), however, the latter may be pre-orogenic for several reasons.

(1) The steep faults appear to have various dip and sense of dip: some of them are normal faults others are reverse ones (**Fig. 4**). This geometry is not predicted in the model by Casas et al. (2003), where steep faults are due to distributed deformation during fault bend folding. On the contrary, if these faults are inherited, they may have been deformed and curved during shortening, especially if they were not reactivated (e.g., Marquer et al., 2006; Lafosse et al., 2016).

(2) In the Casas et al. (2003) kinematical model, the steep faults form lately in the basement, after the initiation of the underlying Bielsa basement thrust. The steep faults form because the basement unit deforms as a fault-bend fold over a flat-ramp system. In this model, to initiate the steep faults, the displacement along the thrust must be at least about the distance between the northernmost and the southernmost steep fault. This would imply a displacement of at least 5 km that is unlikely for a thrust that is poorly constrained by structural mapping. Recent structural interpretations do not include any flat structures (e.g., Jolivet et al., 2007).

(3) The Bielsa unit is affected by horizontal deformation characterized by basement-cover interface antiforms associated with distributed basement deformation. These deformations cannot result from fault-bend fold-associated deformation as in Casas et al. (2003), as such kinematics do not require the formation of a pervasive axial plane foliation. It appears that such contractional deformation is quite systematically present in the hangingwall of steep faults (or northern block when the faults are reverse and north-verging). This suggests that there might be a genetic link between the steep faults and the basement-cover interface antiforms: the latter may localize close to the former. In this case, it would be clear that the steep faults have to be inherited to influence the location of the Cenozoic contractional structures.

(4) In the model of Casas et al. (2003), the steep faults being late, they must deform the overlying nappe (Millares). However, in the field the latter does not appear as folded/deformed by steep faults (**Fig. 7a**): The basal thrust of the Millares nappe is only affected by open, large-wavelength folding although below, the Triassic layers are strongly folded.

(5) Extension is known to have occurred in the Pyrenees Axial Zone at various times: during the Stephano-Permian (Saura et al., 2006) and during the mid-Cretaceous (Johnson et al., 1996). These extensions may have triggered the formation of steep normal faults. Johnson et al. (1996) showed that mineralizations in veins, in the same basement unit further East in the Pyrenees, formed during Mesozoic extension with fluid flowing downward along normal faults.

To sum up, we have shown that the steep faults may have been inherited from pre-orogenic stages, thus supporting our cross-sectional restoration (**Fig. 4**). However, we cannot exclude the fact that these steep faults have been reactivated during the late basement deformation as suggested in Casas et al. (2003).

403

404 6.2. Inherited thermal structure

405 RSCM data, chlorite thermometry as well as thermochronologic data show that the thermal
406 peak is about 300 +/- 30 °C for the Gavarnie unit and around 250 +/- 30 °C for the Bielsa,
407 consistent with Jolivet et al. (2007) and with Ar/Ar step heating data on late Variscan biotites
408 and their likely partial resetting during the Pyrenean orogeny (Jolivet et al., 2007), in addition
409 to temperatures deduced from fluid inclusions and petrography in the Eaux Chaudes shear
410 zones (Henderson and McCaig, 1996; Ingles et al., 1999).

411 These temperatures are very high considering the inferred sedimentary and tectonic burial of
412 both massifs. For the Bielsa unit basement, reasonable estimates of sedimentary burial are
413 about 1 km of Mesozoic and Paleocene formations plus 3 km of Eocene turbidites (Labaume
414 et al., 1985). Such a thin overburden would require a very high geothermal gradient, of about
415 70°C/km, in order to attain 300° C at the cover-basement interface. Thus, it is very unlikely
416 that the recorded Tmax characterizes the temperature at the cover base during the turbidite
417 basin formation. If we consider the Eocene tectonic burial following the turbiditic basin, a
418 thickness of about 5 km (basement and cover of the Gavarnie unit, see cross-sections in
419 Jolivet et al., 2007; with an uncertainty of about 1 km) plus Bielsa cover (only 1 km as the
420 Eocene turbidites were detached before the Gavarnie unit emplaced above the Bielsa unit), we
421 obtain a burial of about 6 km +/- 1 km; this implies a geothermal gradient of at least 45 +/- 10
422 °C/km.

423 Similarly, the sedimentary cover of the Gavarnie basement is too thin to explain the
424 estimated Tmax. The tectonic burial may have been about 2 km +/- 0.5 km (see cross-sections
425 in Teixell, 1996). If we add the thickness of the Gavarnie unit above the analyzed samples and
426 below the Lakora unit (4 km +/- 1 km), we obtain a maximum thickness of about 6 km +/- 1.5
427 km, hence a geothermal gradient of 50 +/- 15 °C/km.

428 Thus, it appears that the geothermal gradients are quite high, the Neouvielle gradient being
429 probably higher than the Bielsa one. However, it is possible that both gradients are similar
430 given the uncertainties. Our results still strongly suggest that both gradients are higher-than-
431 normal (i.e., higher than 25-30 °C/km) and that the Neouvielle gradient is slightly higher than
432 the Bielsa one.

433 Such geothermal gradients are Eocene to post-Eocene in age as they were determined from
434 thermochronologic data yielding Eocene to Oligocene ages and from thermo(baro)metry on
435 phyllosilicates that are at least partly Alpine in age, given that their deformations are
436 kinematically consistent with the deformation in the Triassic meta-sediments. In the North
437 Pyrenean Zone (NPZ), an early Eocene gradient of about 70-80 °C/km was determined
438 (Vacherat et al., 2014) and interpreted as the consequence of Albo-Cenomanian thinning that
439 occurs in the NPZ. The thermal anomaly reached a climax as oceanic spreading started in the
440 Bay of Biscay at 100 Ma. This led to a profound and durable change in the thermal structure
441 of northern Iberia margin lithosphere (Rat et al., 2019) until the plate convergence started.
442 Our results suggest that the thermal anomaly due to mid-Cretaceous rifting processes lasted
443 long enough to be still active during Eocene shortening and that it was large (in space)
444 enough to affect the Iberian crust that was only moderately thinned (i.e., in the future Axial
445 Zone, **Fig. 18**).

446 The rifting event probably stopped around 95 Ma and convergence started just after this
447 event (Mouthereau et al., 2014 and references therein). Considering that shortening recorded
448 in the western Axial Zone probably started around 55 Ma, the thermal anomaly inherited from
449 the rifting stage lasted about 40 Ma. This time interval being quite long, it may suggest that a
450 small-scale sub-lithospheric convection was active in this area, at least until the convergence
451 started at about 80 Ma. This may indeed occur at the rift margins as proposed by Boutillier
452 and Keen (1999) and may have triggered partial melting (van Wijk et al., 2001).

453 The fact that the crust may have suffered a high thermal gradient while it was not
454 significantly thinned may be explained as follows: the lithosphere base is most likely thinned
455 with a wavelength much higher than that affecting the crust, as it is thicker. Such
456 characteristic length is probably about 200-300 km. As a consequence, the lithospheric
457 thermal gradient, controlled by the lithosphere base isotherms, may be affected by thermal
458 anomalies in an area much larger than the area of crustal thinning (**Fig. 18**). This suggests that
459 the thermal anomaly in a lithosphere due to thinning may not be restricted to the area of
460 crustal thinning, i.e., the margin. Such interpretations are in line with models of depth
461 dependent extension (Royden and Keen, 1980) where the crust is less stretched and thinned
462 than the mantle in some margins as suggested by subsidence data (Royden and Keen, 1980;
463 Davis and Kusznir, 2003) and reproduced in thermo-mechanical models (e.g., Huismans and
464 Beaumont, 2011). In the distal part of the rift, the crust is more thinned than the mantle (as in
465 other distal margins, e.g., Peron Pinvidic et al., 2013 and references therein) as attested by

466 mantle exhumation in the rift center (Lagabrielle and Bodinier, 2008; Lagabrielle et al., 2010;
467 Clerc et al., 2012; 2014; Jammes et al., 2009; Masini et al., 2014). In the more proximal part
468 of the rift, the crust is less thinned than the mantle as in many margins worldwide (e.g., Davis
469 and Kusznir, 2004 and references therein).

470

471 6.3. Thermal and structural evolution

472 The Eaux Chaudes shear zone was active at about 48 +/- 2 Ma (Wayne and McCaig, 1998).
473 Similarly, further East the Merens shear zone was reactivated around 48 Ma (Mc Caig and
474 Miller, 1989). The Larra thrust, linked to the Lakora thrust was active until about 40-45 Ma
475 (Teixell, 1996). Thus, between 50 and 40 Ma, several shear zones/thrusts were active in the
476 Gavarnie/Lakora unit. It is noteworthy that it corresponds to the probable exhumation during
477 Eocene times suggested by ZFT data (see above). The emplacement of these thrust/shear
478 zones (Lakora and Eaux Chaudes) did not thicken the crust significantly (see cross-sections in
479 Teixell, 1996). Moreover, it implies that these thrusts were probably not the main control on
480 the Hecho turbidite basin development. It is possible that this basin was a lateral basin (West
481 of the proto-Pyrenees) due to crustal thickening further east in central Pyrenees where the
482 orogen started to grow earlier (see references above). Since 50-55 Ma, the Gavarnie unit was
483 buried below the Hecho turbiditic basin. However, at about 50 Ma, we record the first
484 shortening, implying that the Gavarnie unit was probably the northern part of the turbiditic
485 basin already slowly exhuming and deforming (Eaux Chaudes shear zones, Wayne and
486 McCaig, 1998) during the deposition of the turbidites. Recently, the Pic de Port Vieux,
487 associated to the Gavarnie thrust has been dated to 37 Ma by Ar/Ar step heating on
488 muscovites (Elmola et al., 2018). This shows that distributed shortening along with
489 exhumation predated the localization of the shortening on the Gavarnie thrust at 37 Ma (**Fig.**
490 **17, 19**).

491 The emplacement of the Gavarnie unit also influenced the burial of Bielsa unit when the
492 Gavarnie thrust became active, around 37 Ma. At this time, the intra-Bielsa deformations (the
493 distributed shortening described in this study) were probably already active (30-40 Ma, **Fig.**
494 **19**). The Guarga thrust activation and the exhumation of the Guarga-Bielsa probably started
495 around 30 Ma. The age of 30 Ma also corresponds to the basinward localization of the Jaca
496 basin, in the Rio Guarga syncline interpreted as the consequence of the Guarga unit
497 emplacement (see Teixell, 1996). This suggests that in the western axial zone a distributed

phase of shortening generally predated the activation of each main thrust (Gavarnie and Guarga).

Such distributed then localized mode of shortening is similar to the modes of shortening characterized in the Alpine External Crystalline Massifs (ECM) where distributed shear zones were active during Oligo-Miocene times (e.g., Marquer et al., 2006; Rolland et al., 2008; Simon-Labric et al., 2009; Sanchez et al., 2011; Bellahsen et al., 2012; 2014; Bellanger et al., 2015, Lacombe and Bellahsen, 2016; Egli et al., 2016; Egli et al., 2017; Mair et al., 2018) before the activation of frontal crustal thrusts (Bellahsen et al., 2014). In the ECM, the deformation occurred under green schist facies metamorphism, at around 300-350°C (Crouzet et al., 2001; Bellanger et al., 2015; Boutoux et al., 2016), thus at temperatures slightly higher than in the Axial Zone. In the External Alps, such mid-crustal temperatures and the associated distributed shortening are due to significant burial below the internal units that thermally weakened the crust (e.g., Butler et al., 2006; Bellahsen et al., 2012). Indeed, in the External Alps, the Alpine mylonites consist of brittle-ductile shear zones that affect various Variscan rocks (migmatic gneisses, micaschists, granites …) where quartz are both fractured and ductily deformed (e.g., Leloup et al., 2005; Rolland et al., 2008; Bellahsen et al., 2012; Bellanger et al., 2014). In the Pyrenean Axial Zone, the mylonites are also brittle-ductile but the rock ductility is mainly due to the diffuse deformation of small-grain micas aggregates. This suggests that periods of distributed shortening may be inherent to early times of mountain building, predating the activity of the main thrusts.

6.4. Sericitization and rheological implications

White micas here have crystallized following destabilization of K-feldpar and plagioclase. Such destabilization is commonly described in shear zones, even in the upper crust (e.g., Wibberley, 1999), where it reduces the strength and increases the ductility of deforming rocks. Such syn-kinematic micas are observed in thin sections presented above (**Fig. 13**c). Undeformed, sericitized samples show that a significant amount of micas likely formed before a deformation, as suggested by sericitized, undeformed samples (**Fig. 13a**). The white micas in these undeformed samples are in textural equilibrium with chlorites (**Fig. 14c**), showing temperatures of about 250°C (**Fig. 16, Table 1**). Therefore, these micas formed most likely after tectonic burial, at the thermal peak, before significant deformation.

529 The fluids responsible for the feldspar destabilization are probably of meteoric origin as is
530 usually the case in the upper crust (e.g., Sibson et al., 1975) and suggested for the area
531 (Henderson and McCaig, 1996). These surficial fluids may have circulated in the rocks
532 through Mesozoic (extensive) fractures (Johnson et al., 1996). The fluids may also be the
533 product of prograde dehydration processes but the protolith contained quite little hydrated
534 phases.

535 Having stressed that sericitization was pre-kinematic implies that the crust was weak since
536 the onset of shortening. Indeed, localization of deformation along interconnected layers of
537 micas reduces the bulk strength of the granodiorites to values close to those of pure mica
538 aggregates (Handy, 1994), that are much lower than those of quartz and feldspar (**Fig. 20**).
539 Given the geothermal gradient determined above, the "brittle" crust was probably about 7-8
540 km thick and its strength may have been controlled by the one of interconnected layers of
541 weak materials (e.g., Bos and Spiers, 2002). Considering a high geothermal gradient and the
542 associated flow law, the crustal strength in the Pyrenean Axial Zone during Cenozoic might
543 have been much lower than a "normal" crustal strength (**Fig. 20**). This weak crustal strength
544 is a likely cause for the distributed deformation that may have been active before the
545 localization of the shortening on crustal ramps (**Fig. 19**), although we still lack
546 geochronologic data to confirm it.

547

548 **Conclusions**

549 This contribution presents field data on the structural evolution of the Bielsa basement unit
550 together with new thermometric and thermochronologic data to constrain the thermal peak. In
551 the basement of the Bielsa unit, shortening is distributed. It consists of several short-
552 wavelength (<1 km) antiforms and synforms affecting the basement top. At outcrop scale,
553 shortening is accommodated by brittle and brittle-ductile shear zones active under greenschist
554 metamorphic conditions. These conditions are attested by temperatures around 250-300°C
555 given by thermometric data and RSCM data, consistent with ZFT ages. At microscale, the
556 protolith is characterized by hydrated phases (mostly phyllosilicates) that strongly influence
557 the mode of shortening at this scale: feldspars are sericitized even in undeformed samples.
558 Sericitization also increases with increasing strain attesting for syn-kinematic feldspar
559 destabilization. We conclude that the high thermal gradient, together with phyllosilicate

560 crystallization, probably induced crustal weakening that controlled the style and timing of
561 shortening.

562

563 **Acknowledgments**

564 This study has been funded by the ANR Pyramid and ISTeP funds. F. Roure and G. Molli
565 are thanked for their suggestions that improved the manuscript.

566

567 **References**

568 Beaumont, C., Muñoz, J.A., Hamilton, J. and Fullsack, P., 2000. Factors controlling the
569 Alpine evolution of the central Pyrenees inferred from a comparison of observations and
570 geodynamical models. Journal of Geophysical Research: Solid Earth, 105(B4), pp.8121-
571 8145.

572 Bellahsen, N., Jolivet, L., Lacombe, O., Bellanger, M., Boutoux, A., Garcia, S., Mouthereau,
573 F., Le Pourhiet, L. and Gumiaux, C., 2012. Mechanisms of margin inversion in the
574 external Western Alps: Implications for crustal rheology. Tectonophysics, 560, pp.62-83.

575 Bellahsen, N., Mouthereau, F., Boutoux, A., Bellanger, M., Lacombe, O., Jolivet, L. and
576 Rolland, Y., 2014. Collision kinematics in the western external Alps. Tectonics, 33(6),
577 pp.1055-1088.

578 Bellanger, M., Augier, R., Bellahsen, N., Jolivet, L., Monié, P., Baudin, T. and Beyssac, O.,
579 2015. Shortening of the European Dauphinois margin (Oisans Massif, Western Alps): New
580 insights from RSCM maximum temperature estimates and 40Ar/39Ar in situ dating.
581 Journal of Geodynamics, 83, pp.37-64.

582 Beyssac, O., Goffé, B., Chopin, C. and Rouzaud, J.N., 2002. Raman spectra of carbonaceous
583 material in metasediments: a new geothermometer. Journal of metamorphic Geology,
584 20(9), pp.859-871.

585 Beyssac, O., Bollinger, L., Avouac, J.P. and Goffé, B., 2004. Thermal metamorphism in the
586 lesser Himalaya of Nepal determined from Raman spectroscopy of carbonaceous material.
587 Earth and Planetary Science Letters, 225(1-2), pp.233-241.

588 Beyssac, O., Simoes, M., Avouac, J.P., Farley, K.A., Chen, Y.G., Chan, Y.C. and Goffé, B.,
589 2007. Late Cenozoic metamorphic evolution and exhumation of Taiwan. Tectonics, 26(6).

590 Bos, B. and Spiers, C.J., 2002. Frictional-viscous flow of phyllosilicate-bearing fault rock:
591 Microphysical model and implications for crustal strength profiles. Journal of Geophysical
592 Research: Solid Earth, 107(B2), 10.1029/2001JB000301

593 Boutilier, R.R. and Keen, C.E., 1999. Small-scale convection and divergent plate boundaries.
594 Journal of Geophysical Research: Solid Earth, 104(B4), pp.7389-7403.

595 Boutoux A., Bellahsen N, Nanni U., Pik R., Rolland Y., Verlaguet A. and Lacombe O.,2016.
596 Thermal and structural evolution of a collisional wedge: insights from U-Th-Sm/He
597 thermochronology and RSCM thermometry in the Aiguilles Rouges/Mont Blanc
598 massifs, Western Alps. Tectonophysics, 683, 109-123

599 Brace, W.F. and Kohlstedt, D.L., 1980. Limits on lithospheric stress imposed by laboratory
600 experiments. Journal of Geophysical Research: Solid Earth, 85(B11), pp.6248-6252.

601 Butler, R.W.H., Casey, M., Lloyd, G.E., Bond, C.E., McDade, P., Shipton, Z. and Jones, R.,
602 2002. Vertical stretching and crustal thickening at Nanga Parbat, Pakistan Himalaya: a
603 model for distributed continental deformation during mountain building. Tectonics, 21(4).

604 Butler, R.W., Tavarnelli, E. and Grasso, M., 2006. Structural inheritance in mountain belts: an
605 Alpine–Apennine perspective. Journal of Structural geology, 28(11), pp.1893-1908.

606 Butler, R.W. and Mazzoli, S., 2006. Styles of continental contraction: A review and
607 introduction. Special papers-Geological Society of America, 414(1).

608 Byerlee, J., 1978. Friction of rocks. In Rock friction and earthquake prediction (pp. 615-626).
609 Birkhäuser, Basel.

610 Carminati, E., 2009. Neglected basement ductile deformation in balanced-section restoration:
611 an example from the Central Southern Alps (Northern Italy). Tectonophysics, 463(1-4),
612 pp.161-166.

613 Carpenter, B.M., Marone, C. and Saffer, D.M., 2011. Weakness of the San Andreas Fault
614 revealed by samples from the active fault zone. Nature Geoscience, 4(4), p.251.

615 Casas, A.M., Oliva, B., Román-Berdiel, T. and Pueyo, E., 2003. Basement deformation:
616 tertiary folding and fracturing of the Variscan Bielsa granite (Axial zone, central
617 Pyrenees). Geodinamica acta, 16(2-6), pp.99-117.

618 Ciesielczuk, J. & Janeczek, J. (2004) Hydrothermal alteration of the Strzelin granite, SW
619 Poland. Journal of Mineralogy and Geochemistry, 179, 239-264

620 Clerc, C., Lagabrielle, Y., Neumaier, M., Reynaud, J.Y. and de Saint Blanquat, M., 2012.
621 Exhumation of subcontinental mantle rocks: evidence from ultramafic-bearing clastic
622 deposits nearby the Lherz peridotite body, French Pyrenees. Bulletin de la Société
623 géologique de France, 183(5), pp.443-459.

624 Clerc, C. and Lagabrielle, Y., 2014. Thermal control on the modes of crustal thinning leading
625 to mantle exhumation: Insights from the Cretaceous Pyrenean hot paleomargins. Tectonics,
626 33(7), pp.1340-1359.

627 Cochelin, B., Chardon, D., Denèle, Y., Gumiaux, C. and Le Bayon, B., 2017. Vertical strain
628 partitioning in hot Variscan crust: Syn-convergence escape of the Pyrenees in the Iberian-
629 Armorican syntax. BSGF, 188, 39, doi.org/10.1051/bsgf/2017206.

630 Cochelin, B., Lemirre, B., Denèle, Y., de Saint Blanquat, M., Lahfid, A. and Duchêne, S.,
631 2018. Structural inheritance in the Central Pyrenees: the Variscan to Alpine
632 tectonometamorphic evolution of the Axial Zone. Journal of the Geological Society,
633 175(2), pp.336-351.

634 Collettini, C., Viti, C., Smith, S.A. and Holdsworth, R.E., 2009a. Development of
635 interconnected talc networks and weakening of continental low-angle normal faults.
636 Geology, 37(6), pp.567-570.

637 Collettini, C., Niemeijer, A., Viti, C. and Marone, C., 2009b. Fault zone fabric and fault
638 weakness. Nature, 462(7275), p.907.

639 Crouzet, C., Ménard, G. and Rochette, P., 2001. Cooling history of the Dauphinoise Zone
640 (Western Alps, France) deduced from the thermopaleomagnetic record: geodynamic
641 implications. Tectonophysics, 340(1-2), pp.79-93.

642 Davis, M. and Kusznir, N.J., 2004. Depth-dependent lithospheric stretching at rifted
643 continental margins. Proceedings of NSF Rifted Margins Theoretical Institute, 136, pp.92-
644 137.

645 Denele, Y., Olivier, P., Gleizes, G. and Barbey, P., 2007. The Hospitalet gneiss dome
646 (Pyrenees) revisited: lateral flow during Variscan transpression in the middle crust. Terra
647 Nova, 19(6), pp.445-453.

648 Denèle Y, Olivier P, Gleizes G. 2008. Progressive deformation of a zone of magma transfer in
649 a transpressional regime: The Variscan Mérens shear zone (Pyrenees, France). Journal of
650 Structural Geology 30: 1138–1149. DOI: 10.1016/j.jsg.2008.05.006.

651 Dubacq, B., Vidal, O. and De Andrade, V., 2010. Dehydration of dioctahedral aluminous
652 phyllosilicates: thermodynamic modelling and implications for thermobarometric
653 estimates. Contributions to Mineralogy and Petrology, 159(2), p.159.

654 Egli, D., Müller, W. and Mancktelow, N., 2016. Laser-cut Rb–Sr microsampling dating of
655 deformational events in the Mont Blanc-Aiguilles Rouges region (European Alps). Terra
656 nova, 28(1), pp.35-42.

657 Egli, D., Mancktelow, N. and Spikings, R., 2017. Constraints from 40Ar/39Ar geochronology
658 on the timing of Alpine shear zones in the Mont Blanc-Aiguilles Rouges region of the
659 European Alps. Tectonics, 36(4), pp.730-748.

660 Elmola, A.A., Buatier, M., Monié, P., Labaume, P., Trap, P. and Charpentier, D., 2018.
661 40Ar/39Ar muscovite dating of thrust activity: a case study from the Axial Zone of the
662 Pyrenees. Tectonophysics, 745, pp.412-429.

663 Espurt N., P. Angrand, A. Teixell, P. Labaume, M. Ford, M. de Saint Blanquat, S. Chevrot.
664 2019. Crustal-scale balanced cross-section and restorations of the Central Pyrenean belt
665 (Nestes-Cinca transect): Highlighting the structural control of Variscan belt and Permian-
666 Mesozoic rift systems on mountain building. Tectonophysics (this issue).
667 doi.org/10.1016/j.tecto.2019.04.026

668 Fitzgerald, P.G., Muñoz, J.A., Coney, P.J. and Baldwin, S.L., 1999. Asymmetric exhumation
669 across the Pyrenean orogen: implications for the tectonic evolution of a collisional orogen.
670 Earth and Planetary Science Letters, 173(3), pp.157-170.

671 Gabalda, S., Beyssac, O., Jolivet, L., Agard, P. and Chopin, C., 2009. Thermal structure of a
672 fossil subduction wedge in the Western Alps. Terra Nova, 21(1), pp.28-34.

673 Galbraith, R.F. and Laslett, G.M., 1993. Statistical models for mixed fission track ages.
674 Nuclear tracks and radiation measurements, 21(4), pp.459-470.

675 Gibson, M., Sinclair, H.D., Lynn, G.J. and Stuart, F.M., 2007. Late-to post-orogenic
676 exhumation of the Central Pyrenees revealed through combined thermochronological data
677 and modelling. Basin Research, 19(3), pp.323-334.

678 Gleizes, G., Leblanc, D. and Bouchez, J.L., 1998. The main phase of the hercynian orogeny
679 of the Pyrenees is a dextral transpression. In: Holdsworth R.E., Stracham R.A., Dewey J.F.
680 (Eds.), Continental Transpressionnal and Transtensional Tectonics. Geological Society of
681 London, special paper, 135, 267-273.

682 Gleizes, G., Leblanc, D., Olivier, P. and Bouchez, J., 2001. Strain partitioning in a pluton
683 during emplacement in transpressional regime: the example of the Néouvielle granite
684 (Pyrenees). International Journal of Earth Sciences, 90(2), pp.325-340.

685 Gueydan, F., Leroy, Y.M., Jolivet, L. and Agard, P., 2003. Analysis of continental midcrustal
686 strain localization induced by microfracturing and reaction-softening. Journal of
687 Geophysical Research: Solid Earth, 108(B2).

688 Handy, M.R., 1994. Flow laws for rocks containing two non-linear viscous phases: a
689 phenomenological approach. Journal of Structural Geology, 16(3), pp.287-302.

690 Handy, M.R., Hirth, G. and Bürgmann, R., 2007. Continental fault structure and rheology
691 from the frictional-to-viscous transition downward. Tectonic Faults: Agents of Change on
692 a Dynamic Earth, pp.139-81.

693 Henderson, I.H.C. and McCaig, A.M., 1996. Fluid pressure and salinity variations in shear
694 zone-related veins, central Pyrenees, France: implications for the fault-valve model.
695 Tectonophysics, 262(1-4), pp.321-348.

696 Holdsworth, R.E., Van Diggelen, E.W.E., Spiers, C.J., De Bresser, J.H.P., Walker, R.J. and
697 Bowen, L., 2011. Fault rocks from the SAFOD core samples: Implications for weakening
698 at shallow depths along the San Andreas Fault, California. Journal of Structural Geology,
699 33(2), pp.132-144.

700 Huismans, R. and Beaumont, C., 2011. Depth-dependent extension, two-stage breakup and
701 cratonic underplating at rifted margins. Nature, 473(7345), p.74.

702 Huyghe, D., Mouthereau, F., Castelltort, S., Filleaudeau, P.Y. and Emmanuel, L., 2009.
703 Paleogene propagation of the southern Pyrenean thrust wedge revealed by finite strain
704 analysis in frontal thrust sheets: Implications for mountain building. Earth and Planetary
705 Science Letters, 288(3-4), pp.421-433.

706 Ingles, J., Lamouroux, C., Soula, J.C., Guerrero, N. and Debat, P., 1999. Nucleation of ductile
707 shear zones in a granodiorite under greenschist facies conditions, Néouvielle massif,
708 Pyrenees, France. Journal of Structural Geology, 21(5), pp.555-576.

709 Jammes, S., Manatschal, G., Lavier, L. and Masini, E., 2009. Tectonosedimentary evolution
710 related to extreme crustal thinning ahead of a propagating ocean: Example of the western
711 Pyrenees. Tectonics, 28(4).

712 Janecke, S.U. and Evans, J.P., 1988. Feldspar-influenced rock rheologies. Geology, 16(12),
713 pp.1064-1067.

714 Jefferies, S.P., Holdsworth, R.E., Wibberley, C.A.J., Shimamoto, T., Spiers, C.J., Niemeijer,
715 A.R. and Lloyd, G.E., 2006. The nature and importance of phyllonite development in

716 crustal-scale fault cores: an example from the Median Tectonic Line, Japan. Journal of
717 Structural Geology, 28(2), pp.220-235.

718 Johnson, C.A., Cardellach, E., Tritlla, J. and Hanan, B.B., 1996. Cierco Pb-Zn-Ag vein
719 deposits; isotopic and fluid inclusion evidence for formation during the Mesozoic
720 extension in the Pyrenees of Spain. Economic Geology, 91(3), pp.497-506.

721 Jolivet, M., Labaume, P., Monié, P., Brunel, M., Arnaud, N. and Campani, M., 2007.
722 Thermochronology constraints for the propagation sequence of the south Pyrenean
723 basement thrust system (France-Spain). Tectonics, 26(5).

724 Labaume, P., Séguret, M. and Seyve, C., 1985. Evolution of a turbiditic foreland basin and
725 analogy with an accretionary prism: Example of the Eocene south-Pyrenean basin.
726 Tectonics, 4(7), pp.661-685.

727 Lachenbruch, A.H. and Sass, J.H., 1980. Heat flow and energetics of the San Andreas fault
728 zone. Journal of Geophysical Research: Solid Earth, 85(B11), pp.6185-6222.

729 Lacombe, O and Bellahsen, N., 2016. Thick-skinned tectonics and basement-involved fold-
730 thrust belts. Insights from selected Cenozoic orogens. Geological Magazine, 153(5-6), pp.
731 763-810

732 Lafosse, M., Boutoux, A., Bellahsen, N. and Le Pourhiet, L., 2016. Role of tectonic burial and
733 temperature on the inversion of inherited extensional basins during collision. Geological
734 Magazine, 153(5-6), pp.811-826.

735 Lagabrielle, Y. and Bodinier, J.L., 2008. Submarine reworking of exhumed subcontinental
736 mantle rocks: field evidence from the Lherz peridotites, French Pyrenees. Terra Nova,
737 20(1), pp.11-21.

738 Lagabrielle, Y., Labaume, P. and de Saint Blanquat, M., 2010. Mantle exhumation, crustal
739 denudation, and gravity tectonics during Cretaceous rifting in the Pyrenean realm (SW
740 Europe): Insights from the geological setting of the lherzolite bodies. Tectonics, 29(4).

741 Lahfid, A., Beyssac, O., Deville, E., Negro, F., Chopin, C. and Goffé, B., 2010. Evolution of
742 the Raman spectrum of carbonaceous material in low-grade metasediments of the Glarus
743 Alps (Switzerland). Terra Nova, 22(5), pp.354-360.

744 Lamouroux, C., Debat, P., Deramond, J. and Majeste-Menjoulas, C., 1979. Influence de
745 massifs plutoniques hercyniens dans l'evolution des structures pyreneennes; exemple du
746 massif du Neouvielle. Bulletin de la Société Géologique de France, 7(2), pp.213-220.

747 Marquer, D., Calcagno, P., Barfety, J.C. and Baudin, T., 2006. 3D modeling and kinematics
748 of the external zone of the French Western Alps (Belledonne and Grand Châtelard Massifs,
749 Maurienne Valley, Savoie). Eclogae Geologicae Helvetiae, 99(2), pp.211-222.

750 Mair, D., Lechmann, A., Herwegh, M., Nibourel, L. and Schlunegger, F., 2018. Linking
751 Alpine deformation in the Aar Massif basement and its cover units–the case of the
752 Jungfrau–Eiger mountains (Central Alps, Switzerland). Solid Earth, 9, pp.1099-1122.

753 Masini, E., Manatschal, G., Tugend, J., Mohn, G. and Flament, J.M., 2014. The tectono-
754 sedimentary evolution of a hyper-extended rift basin: the example of the Arzacq–Mauléon
755 rift system (Western Pyrenees, SW France). International Journal of Earth Sciences,
756 103(6), pp.1569-1596.

Mazzoli, S., Vitale, S., Delmonaco, G., Guerriero, V., Margottini, C. and Spizzichino, D., 2009. 'Diffuse faulting'in the Machu Picchu granitoid pluton, Eastern Cordillera, Peru. Journal of Structural Geology, 31(11), pp.1395-1408.

McCaig, A.M. and Miller, J.A., 1986. ^{40}Ar-^{39}Ar age of mylonites along the Merens fault, central Pyrenees. Tectonophysics, 129(1-4), pp.149-172.

Metcalf, J.R., Fitzgerald, P.G., Baldwin, S.L. and Muñoz, J.A., 2009. Thermochronology of a convergent orogen: Constraints on the timing of thrust faulting and subsequent exhumation of the Maladeta Pluton in the Central Pyrenean Axial Zone. Earth and Planetary Science Letters, 287(3-4), pp.488-503.

Mouthereau, F., Filleaudeau, P.Y., Vacherat, A., Pik, R., Lacombe, O., Fellin, M.G., Castelltort, S., Christophoul, F. and Masini, E., 2014. Placing limits to shortening evolution in the Pyrenees: Role of margin architecture and implications for the Iberia/Europe convergence. Tectonics, 33(12), pp.2283-2314.

Morris, R.G., Sinclair, H.D. and Yelland, A.J., 1998. Exhumation of the Pyrenean orogen: implications for sediment discharge. Basin Research, 10(1), pp.69-85.

Muñoz, J.A., 1992. Evolution of a continental collision belt: ECORS-Pyrenees crustal balanced cross-section. In Thrust tectonics (pp. 235-246). Springer, Dordrecht.

Niemeijer, A.R. and Spiers, C.J., 2005. Influence of phyllosilicates on fault strength in the brittle-ductile transition: Insights from rock analogue experiments. Geological Society, London, Special Publications, 245(1), pp.303-327.

Niemeijer, A., Marone, C. and Elsworth, D., 2010. Fabric induced weakness of tectonic faults. Geophysical Research Letters, 37(3).

Olivet, J.L., 1996. La cinématique de la plaque ibérique. Bull. Cent. Rech. Explor. Prod. Elf Aquitaine, 20(1), pp.131-195.

Peron-Pinvidic, G., Manatschal, G. and Osmundsen, P.T., 2013. Structural comparison of archetypal Atlantic rifted margins: A review of observations and concepts. Marine and Petroleum Geology, 43, pp.21-47.

Puigdefàbregas, C. and Souquet, P., 1986. Tecto-sedimentary cycles and depositional sequences of the Mesozoic and Tertiary from the Pyrenees. Tectonophysics, 129(1-4), pp.173-203.

Ranalli, G. and Murphy, D.C., 1987. Rheological stratification of the lithosphere. Tectonophysics, 132(4), pp.281-295.

Rat, J., Mouthereau, F., Brichau, S., Crémades, A., Bernet, M., Balvay, M., Ganne, J., Lahfid, A., Gautheron, C., 2019. Tectonothermal Evolution of the Cameros Basin: Implications for Tectonics of North Iberia. Tectonics 40, 327. doi:10.1029/2018TC005294

Rolland, Y., Rossi, M., Cox, S.F., Corsini, M., Mancktelow, N., Pennacchioni, G., Fornari, M. and Boullier, A.M., 2008. 40Ar/39Ar dating of synkinematic white mica: insights from fluid-rock reaction in low-grade shear zones (Mont Blanc Massif) and constraints on timing of deformation in the NW external Alps. Geological Society, London, Special Publications, 299(1), pp.293-315.

Román-Berdiel, T., Casas, A.M., Oliva-Urcia, B., Pueyo, E.L. and Rillo, C., 2004. The main Variscan deformation event in the Pyrenees: new data from the structural study of the Bielsa granite. Journal of Structural Geology, 26(4), pp.659-677.

Roure, F., Choukroune, P., Berastegui, X., Munoz, J.A., Villien, A., Matheron, P., Bareyt, M., Seguret, M., Camara, P. and Deramond, J., 1989. ECORS deep seismic data and balanced cross sections: Geometric constraints on the evolution of the Pyrenees. Tectonics, 8(1), pp.41-50.

Royden, L. and Keen, C.E., 1980. Rifting process and thermal evolution of the continental margin of eastern Canada determined from subsidence curves. Earth and Planetary Science Letters, 51(2), pp.343-361.

Sanchez, G., Rolland, Y., Schneider, J., Corsini, M., Oliot, E., Goncalves, P., Verati, C., Lardeaux, J.M. and Marquer, D., 2011. Dating low-temperature deformation by 40Ar/39Ar on white mica, insights from the Argentera-Mercantour Massif (SW Alps). Lithos, 125(1-2), pp.521-536.

Saura, E. and Teixell, A., 2006. Inversion of small basins: effects on structural variations at the leading edge of the Axial Zone antiformal stack (Southern Pyrenees, Spain). Journal of Structural Geology, 28(11), pp.1909-1920.

Scholz, C.H., 1989. Mechanics of faulting. Annual Review of Earth and Planetary Sciences, 17(1), pp.309-334.

Shea Jr, W.T. and Kronenberg, A.K., 1993. Strength and anisotropy of foliated rocks with varied mica contents. Journal of Structural Geology, 15(9-10), pp.1097-1121.

Sibson, R.H., Moore, J.M.M. and Rankin, A.H., 1975. Seismic pumping—a hydrothermal fluid transport mechanism. Journal of the Geological Society, 131(6), pp.653-659.

Simon-Labric, T., Rolland, Y., Dumont, T., Heymes, T., Authemayou, C., Corsini, M. and Fornari, M., 2009. 40Ar/39Ar dating of Penninic Front tectonic displacement (W Alps) during the Lower Oligocene (31–34 Ma). Terra Nova, 21(2), pp.127-136.

Sinclair, H.D., Gibson, M., Naylor, M. and Morris, R.G., 2005. Asymmetric growth of the Pyrenees revealed through measurement and modeling of orogenic fluxes. American Journal of Science, 305(5), pp.369-406.

Teixell, A., 1996. The Ansó transect of the southern Pyrenees: basement and cover thrust geometries. Journal of the Geological Society, 153(2), pp.301-310.

Teixell, A., 1998. Crustal structure and orogenic material budget in the west central Pyrenees. Tectonics, 17(3), pp.395-406.

Teixell, A., Labaume, P., Ayarza, P., Espurt, N., de Saint Blanquat, M. and Lagabrielle, Y., 2018. Crustal structure and evolution of the Pyrenean-Cantabrian belt: A review and new interpretations from recent concepts and data. Tectonophysics, 724, pp.146-170.

Vacherat, A., Mouthereau, F., Pik, R., Bernet, M., Gautheron, C., Masini, E., Le Pourhiet, L., Tibari, B. and Lahfid, A., 2014. Thermal imprint of rift-related processes in orogens as recorded in the Pyrenees. Earth and Planetary Science Letters, 408, pp.296-306.

836 Van Wijk, J.W., Huismans, R.S., Ter Voorde, M. and Cloetingh, S.A.P.L., 2001. Melt
837 generation at volcanic continental margins: no need for a mantle plume? Geophysical
838 Research Letters, 28(20), pp.3995-3998.

839 Vermeesch, P., 2009, RadialPlotter: a Java application for fission track, luminescence and
840 other radial plots, Radiation Measurements, 44, 4, 409-410

841 Vitale Brovarone, A., Beyssac, O., Malavieille, J., Molli, G., Beltrando, M. and Compagnoni,
842 R., 2013. Stacking and metamorphism of continuous segments of subducted lithosphere in
843 a high-pressure wedge: the example of Alpine Corsica (France). Earth-Science Reviews,
844 116, pp.35-56.

845 Vidal, O., De Andrade, V., Lewin, E., Munoz, M., Parra, T. and Pascarelli, S., 2006. P–T-
846 deformation-Fe3+/Fe2+ mapping at the thin section scale and comparison with XANES
847 mapping: application to a garnet-bearing metapelite from the Sambagawa metamorphic
848 belt (Japan). Journal of Metamorphic Geology, 24(7), pp.669-683.

849 Wayne, D.M. and McCaig, A.M., 1998. Dating fluid flow in shear zones: Rb-Sr and U-Pb
850 studies of syntectonic veins in the Néouvielle Massif, Pyrenees. Geological Society,
851 London, Special Publications, 144(1), pp.129-135.

852 Wibberley, C., 1999. Are feldspar-to-mica reactions necessarily reaction-softening processes
853 in fault zones? Journal of Structural Geology, 21(8-9), pp.1219-1227.

854 Wintsch, R.P., Christoffersen, R. and Kronenberg, A.K., 1995. Fluid-rock reaction weakening
855 of fault zones. Journal of Geophysical Research: Solid Earth, 100(B7), pp.13021-13032.

856 Zoback, M.D., Zoback, M.L., Mount, V.S., Suppe, J., Eaton, J.P., Healy, J.H., Oppenheimer,
857 D., Reasenberg, P., Jones, L., Raleigh, C.B. and Wong, I.G., 1987. New evidence on the
858 state of stress of the San Andreas fault system. Science, 238(4830), pp.1105-1111.

859

860 **Acknowledgments**: This project has been funded by ISTeP-Sorbonne Université and ANR
861 Pyramid funds. G. Molli and F. Roure are thanked for their reviews that improved the
862 manuscript.

863

864 **Figure caption**

865

866 Figure 1: Simplified structural map of the Pyrenees. The Axial Zone is located between the
867 North Pyrenean Zone (NPZ) and the South Pyrenean Zone (SPZ). The two main units in the
868 western Axial Zone are the Gavarnie and Bielsa units. The Guarga unit does not crop out and
869 is located below the Bielsa unit and the Jaca basin. The line represents the trace of the cross-
870 section presented in Fig. 2, the box the map in Fig. 3.

Figure 2: Regional cross-section from Jolivet et al. (2007). Four main units are represented in the Axial Zone: the Lakora, the Gavarnie, the Bielsa, and the Guarga units, from north to south, respectively. Shortening in the cover of the South Pyrenean Zone is linked to basement thrusts in the Axial Zone or underneath the Jaca basin.

Figure 3: Geological map of the Bielsa unit after Casas et al. (2003). The Bielsa unit is structurally below the Millares unit. On Fig. 2, Bielsa and Millares units are grouped under Bielsa unit name. The Bielsa unit is composed of a Variscan Carboniferous granite/granodiorite intruding the Paleozoic cover. The Triassic layers unconformably overly the basement. Several WNW-ESE to ENE-WSW antiforms and synforms affect the cover and the basement top. Two klippen of Millares unit (Fobillons and Punta Suelza) are cropping out above the folded cover of Bielsa unit. The line represents the trace of the cross-section presented in Fig. 4, the box the map in Fig. 5.

Figure 4: Cross-section of the Bielsa unit and its restoration. The shortening is estimated considering constant length for Triassic and non-reactivated inherited faults. Nine antiforms are mapped along with 6 steep faults. The restoration is done assuming inherited steep faults (see text for explanation and discussion). However, the age of these faults is poorly constrained as attested by the question marks: the Cretaceous layers are drawn syn-tectonic although it is not necessarily the case. Same legend than Fig. 3.

Figure 5: Structural map of the Lago Urdiceto area. Three steep structures are mapped along the southern limb of the Urdiceto, the Western, and the Punta Suelza synforms. Small scale shear zones are also recognized, as well as an Alpine schistosity/cleavage (in both the basement and cover) mainly steeply north-dipping. These structures and striated faults are consistent with a NNE-SSW contraction. Sites of measurements and sampling are indicated.

899 Figure 6: Cross-sections through Urdiceto synform. See Fig. 5 for location. The synform is
900 bounded northward by a steep normal fault. It is asymmetrical especially in its eastern part,
901 with an overhanging sheared flank. The apparent folding of the top basement is associated to
902 distributed deformation within the basement (e.g., shear zones).

903

904 Figure 7: Field photographs. a) Punta Suelza klippen over the Bielsa unit with folded
905 Triassic layers suggesting a folding during the nappe emplacement. b) The Urdiceto synform
906 (see Fig. 5 and 6). c) The Western synform with the syn-S1 folding.

907

908 Figure 8: Field photographs of the Urdiceto synform basement. a) Altered top basement with
909 penetrative schistosity. b) Zoom on an unaltered granodiorite with less penetrative schistosity.

910

911 Figure 9: Field photographs of reverse top-to-the-South shear zones in the basement.

912

913 Figure 10: Field photographs of the Urdiceto synform cover. a) Basement/Triassic
914 unconformity with bedding-parallel top-to-the-South shearing. b) Sub-vertical cleavage and
915 sub-horizontal veins attesting for horizontal shortening and vertical stretching. c) Fold with
916 steep axial surfaces and associated cleavage.

917

918 Figure 11: Northern contact (steep fault) of the Western synform (see Fig. 5 for location). a)
919 Steep (reverse, South verging) fault and steep cleavage oblique to bedding in the cover. b)
920 Zoom of the cover deformation with locally cleavage parallel to bedding and small-scale
921 reverse faults (South verging).

922

923 Figure 12: Thin-sections photographs. The rocks are composed of quartz, phengite,
924 feldspars, chlorites and some contain calcite a) Polarized (sample B11-33). b) Interpretation
925 (sample B11-33, Fig. 5). The rock is affected by cataclastic deformation. c) Ductile
926 deformation with mylonitic shear zones (sample B11-31, Fig. 5). This foliated rock is

927 composed of fractured quartz, deformed chloritized biotites, calcite, and micrometric white
928 micas.

929

930 Figure 13: Photographs of thin sections. a) Undeformed (except a few fractures) granite with
931 quartz, chlorite (dark crystals), and micas partly replacing feldspars (pseudomorphs) (sample
932 B11-33, Fig. 5). b) protomylonite where quartz are embedded in aggregates of micas and
933 chlorites (dark phases) with the development of a weak schistosity (sample B11-18, Fig. 5). c)
934 Mylonite with fractured quartz, a schistosity (S1) mainly composed of micas, pressure
935 shadows of chlorite/mica around quartz, and formation of a few micro shear zones (sample
936 B11-31, Fig. 5). Between a) and c) the amount of phyllosilicates, in particular micas, strongly
937 increases.

938

939 Figure 14: SEM images of the progressive sericitization. a) Albitisation of K feldspars in a
940 weakly deformed sample (sample B10-31). b) Albitisation and phengitisation of K feldspars,
941 along with titanite and epidotes inclusions in weakly deformed samples (sample B11-33). c)
942 Biotites replaced by micas and chlorites (bright spots: apatites) in an undeformed sample
943 (Quartz and Feldspars) (sample B11-37). d) Quartz embedded in an Albite/micas “matrix”
944 (sample B10-31). e) Images of a phyllonite composed almost exclusively of micas (with
945 quartz out of the image) (sample B11-14).

946

947 Figure 15: Results of thermometric study. For 4 samples, the temperature is provided with 2
948 methods. The multi-equilibrium thermo-barometer on Quartz Micas is from Dubacq et al.
949 (2010). The multi-equilibrium thermo-barometer on chlotite is from Vidal et al. (2006).

950

951 Figure 16: Zircon fission-track data and location of samples. Plots are realized with Radial
952 Plotter (Vermeesch, 2009).

953

954 Figure 17: Speculative thermal structure of the Iberian lithosphere. In the southern part, the
955 thermal structure is considered as normal given its age and the Moho temperature set at

slightly more than 500°C (lithosphere with a thermotectonique age of about 200 Myrs). In the northern part, the thermal structure is built using the gradient of 80 °C/km from Vacherat et al. (2016) in the North Pyrenean Zone. Between these 2 zones, i.e., in the future Axial Zone, the geothermal gradient is intermediate between the northern and the southern one, and fits the gradients of about 50°C/km estimated in this study for the northern axial zone.

Figure 18: Thermal histories for a) Bielsa and b) Neouvielle. See text for explanations.

Figure 19: Present day cross-section of the Pyrenees and possible ages of deformation. The deep structure is from Chevrot et al. (2018). The cover structure in the foreland basin is from Jolivet et al. (2005). For a detailed balanced cross-section and its restored stage see Teixell et al. (2016) and Espurt et al. (this issue). Bielsa thrust and internal Bielsa deformation ages are deduced from discussion on the timing of the other structures (see text).

Figure 20: Rheological laws for both typical continental basement (quartz) and weakened (hot) continental crust. The weakened strength of the upper crust is from Bos and Spiers (2002) for strain rates of both 10^{-10} and 10^{-12} s^{-1}, as the result of sericitized feldspars. The associated lower crust strength is considered for a rather high inherited geothermal gradient of 45 °C/km.

Table 1: Maximal temperatures obtained from RSCM method.

Table 2: Zircon Fission Track dataset from Bielsa and Neouvielle plutonic massifs.

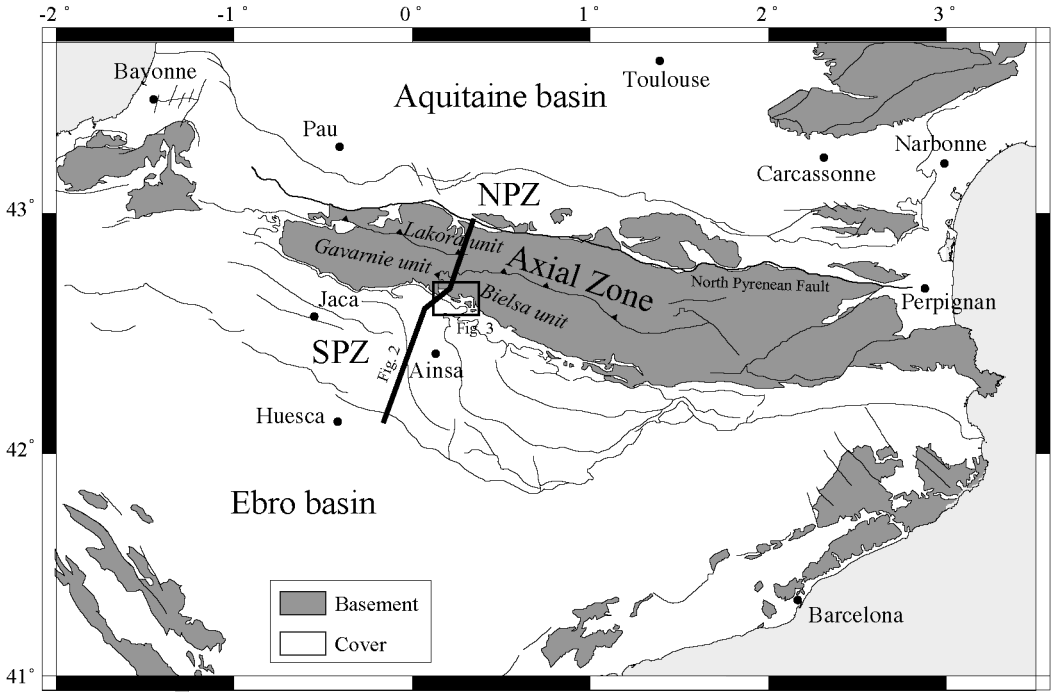
-2 °
-1 °
0 °
1 °
2 °
3 °
43 °
42 °
41 °
Bayonne
Aquitaine basin
Toulouse
Pau
Narbonne
Carcassonne
NPZ
Lakora unit
Gavarnie unit
Axial Zone
North Pyrenean Fault
Jaca
Bielsa unit
Perpignan
Fig. 3
SPZ
Fig. 2
Ainsa
Huesca
Ebro basin
Basement
Cover
Barcelona

Figure 1

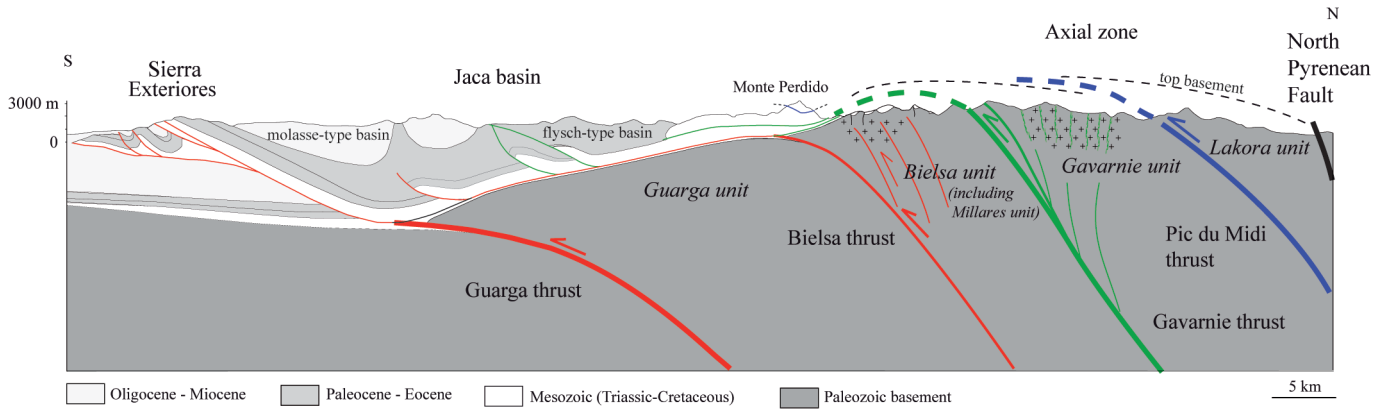
S
N
Sierra
Exteriores
Jaca basin
Monte Perdido
Axial zone
top basement
North
Pyrenean
Fault
3000 m
0
molasse-type basin
flysch-type basin
Guarga unit
Bielsa unit
(including
Millares unit)
Gavarnie unit
Lakora unit
Bielsa thrust
Pic du Midi
thrust
Guarga thrust
Gavarnie thrust
Oligocene - Miocene
Paleocene - Eocene
Mesozoic (Triassic-Cretaceous)
Paleozoic basement
5 km

Figure 2

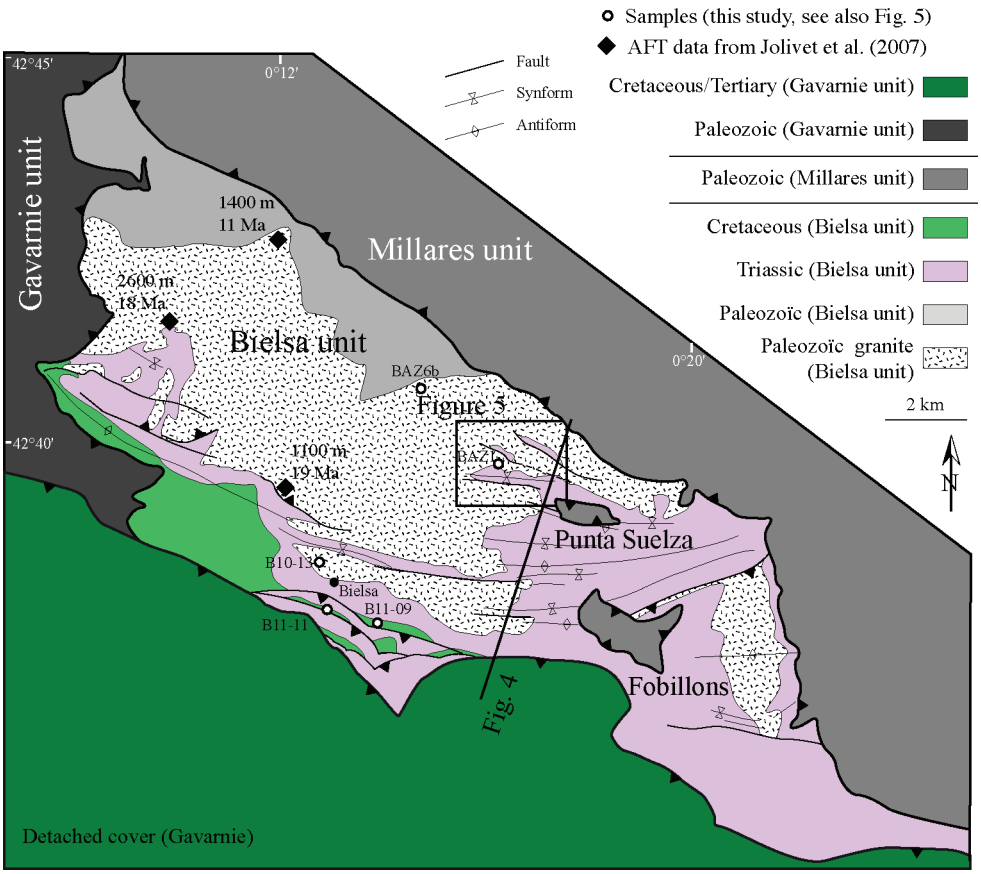
Samples (this study, see also Fig. 5)
AFT data from Jolivet et al. (2007)
Fault
Synform
Antiform
Cretaceous/Tertiary (Gavarnie unit)
Paleozoic (Gavarnie unit)
Paleozoic (Millares unit)
Cretaceous (Bielsa unit)
Triassic (Bielsa unit)
Paleozoïc (Bielsa unit)
Paleozoïc granite (Bielsa unit)
2 km
N
42°45'
0°12'
0°20'
42°40'
Gavarnie unit
Millares unit
Bielsa unit
1400 m
11 Ma
2600 m
18 Ma
1100 m
19 Ma
BAZ6b
BAZ5
Figure 3
Punta Suelza
Fobillons
B10-13
Bielsa
B11-09
B11-11
Fig. 4
Detached cover (Gavarnie)

Figure 3

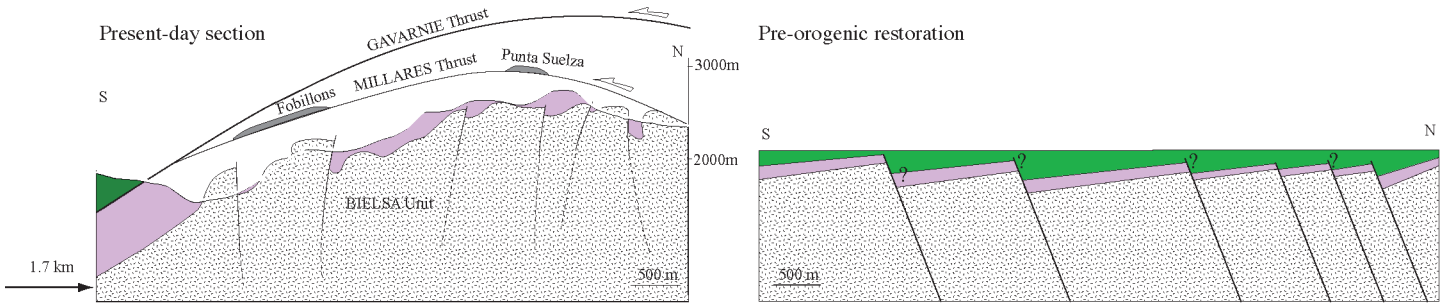
Present-day section
GAVARNIE Thrust
MILLARES Thrust
Punta Suelza
Fobillons
S
N
3000m
2000m
BIELSA Unit
1.7 km
500 m
Pre-orogenic restoration
S
N
?
?
?
?
500 m

Figure 4

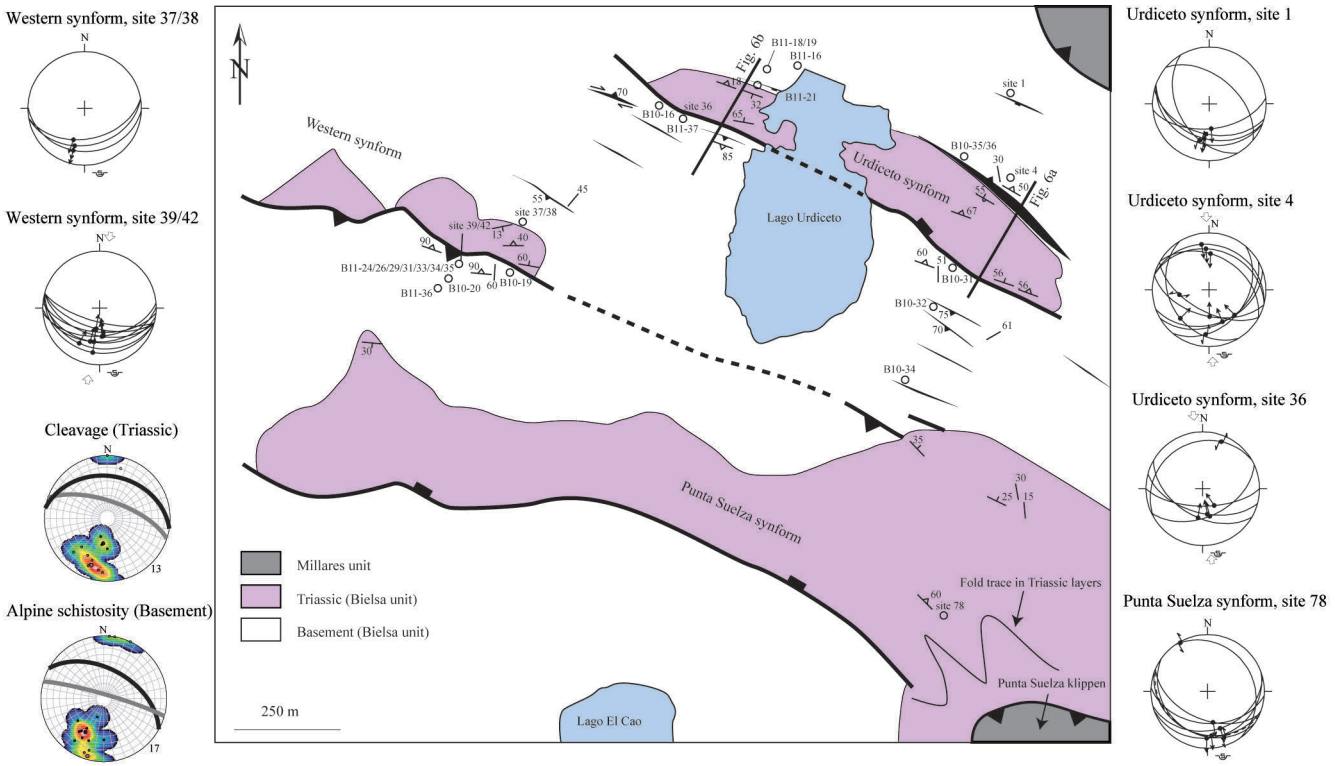
Western synform, site 37/38
Western synform, site 39/42
Cleavage (Triassic)
Alpine schistosity (Basement)
Western synform
Urdiceto synform
Punta Suelza synform
Lago Urdiceto
Lago El Cao
Millares unit
Triassic (Bielsa unit)
Basement (Bielsa unit)
Fold trace in Triassic layers
Punta Suelza klippen
250 m
Urdiceto synform, site 1
Urdiceto synform, site 4
Urdiceto synform, site 36
Punta Suelza synform, site 78

Figure 5

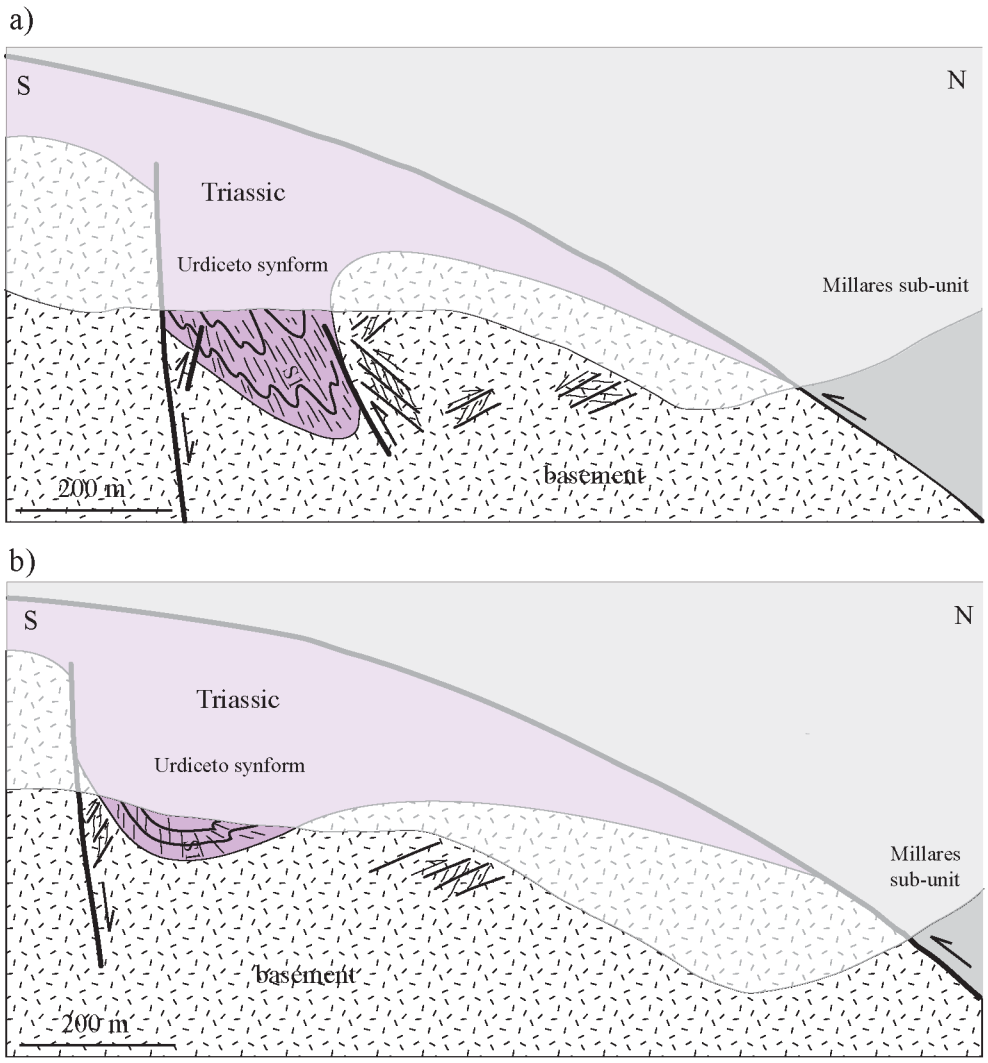
a)
S
N
Triassic
Urdiceto synform
Millares sub-unit
basement
200 m
b)
S
N
Triassic
Urdiceto synform
Millares
sub-unit
basement
200 m

Figure 6

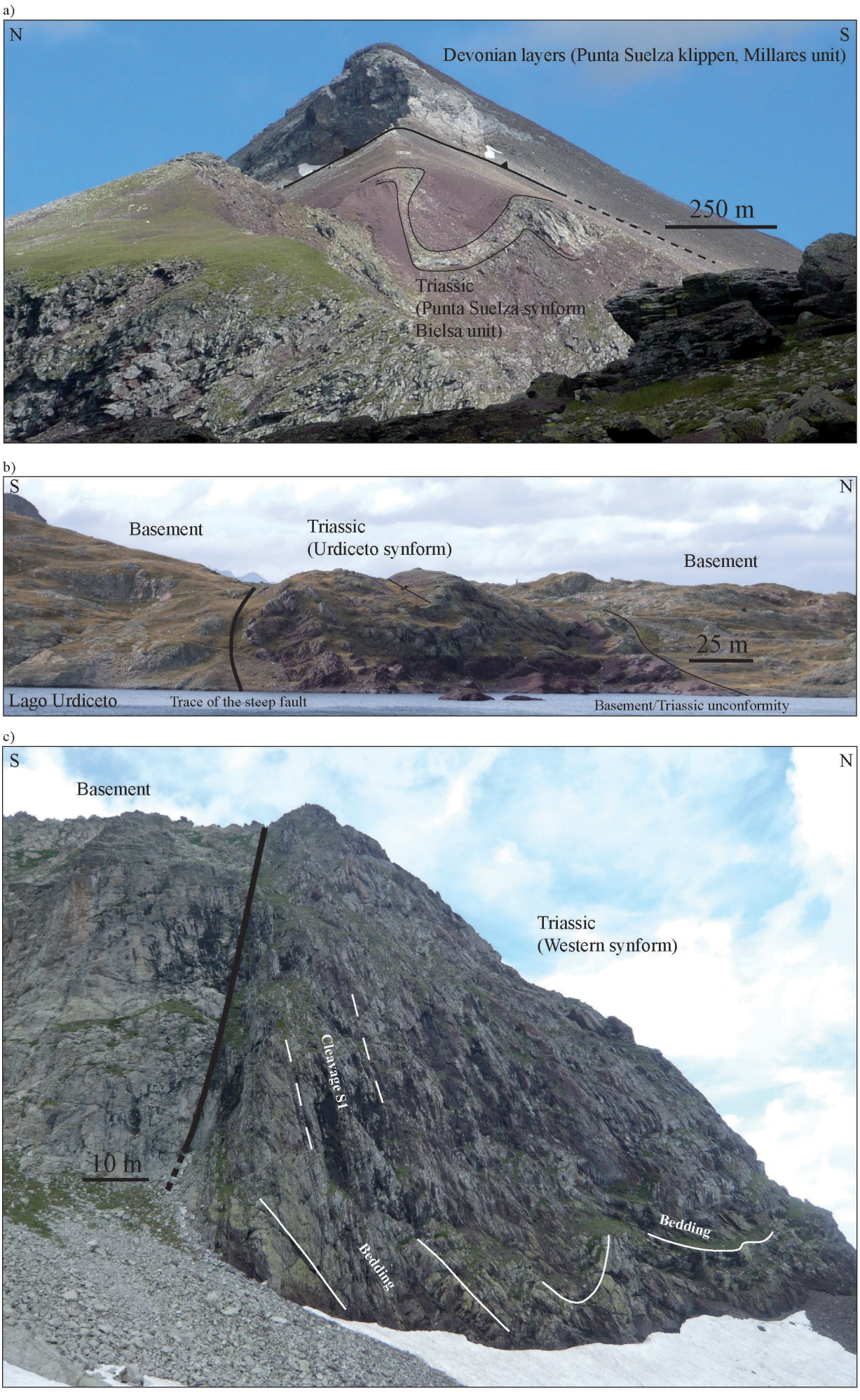
a)
N
S
Devonian layers (Punta Suelza klippen, Millares unit)
250 m
Triassic
(Punta Suelza synform
Bielsa unit)
b)
S
N
Basement
Triassic
(Urdiceto synform)
Basement
25 m
Lago Urdiceto
Trace of the steep fault
Basement/Triassic unconformity
c)
S
N
Basement
Triassic
(Western synform)
Cleavage S1
10 m
Bedding
Bedding

Figure 7

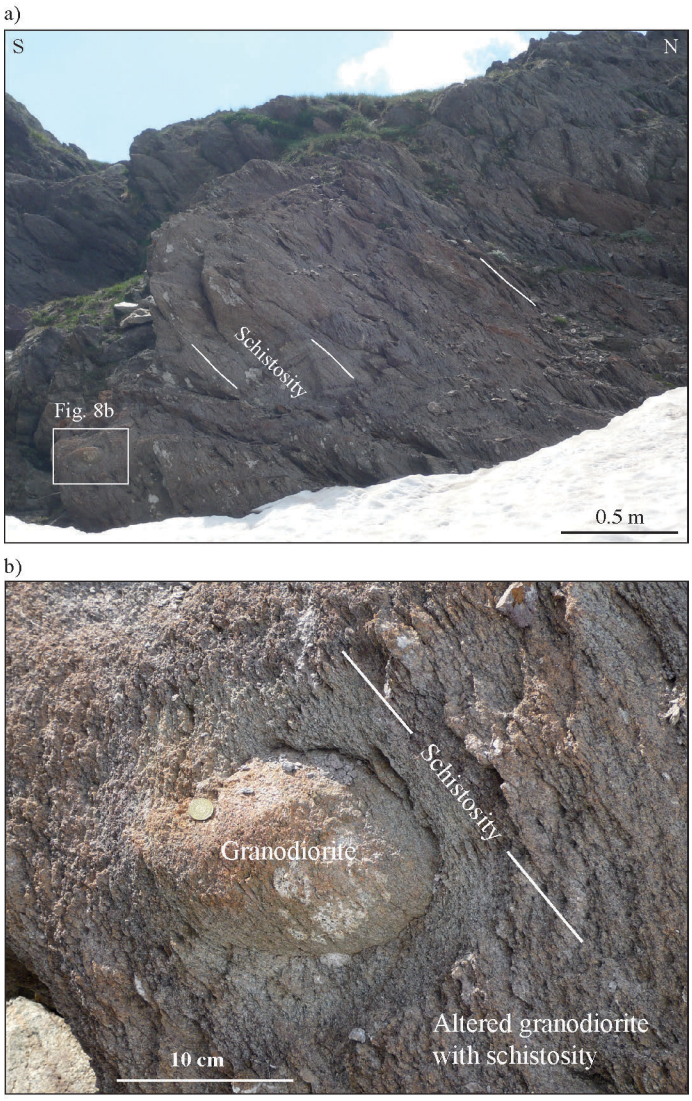
a)
S
N
Schistosity
Fig. 8b
0.5 m
b)
Granodiorite
Schistosity
Altered granodiorite
with schistosity
10 cm

Figure 8

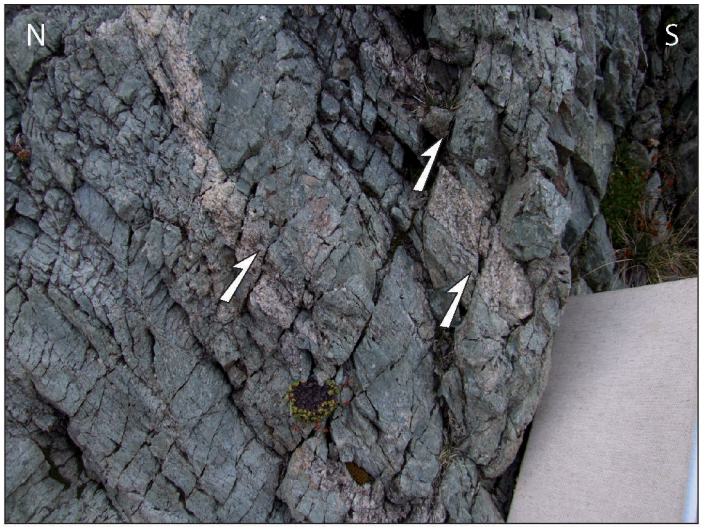

Figure 9

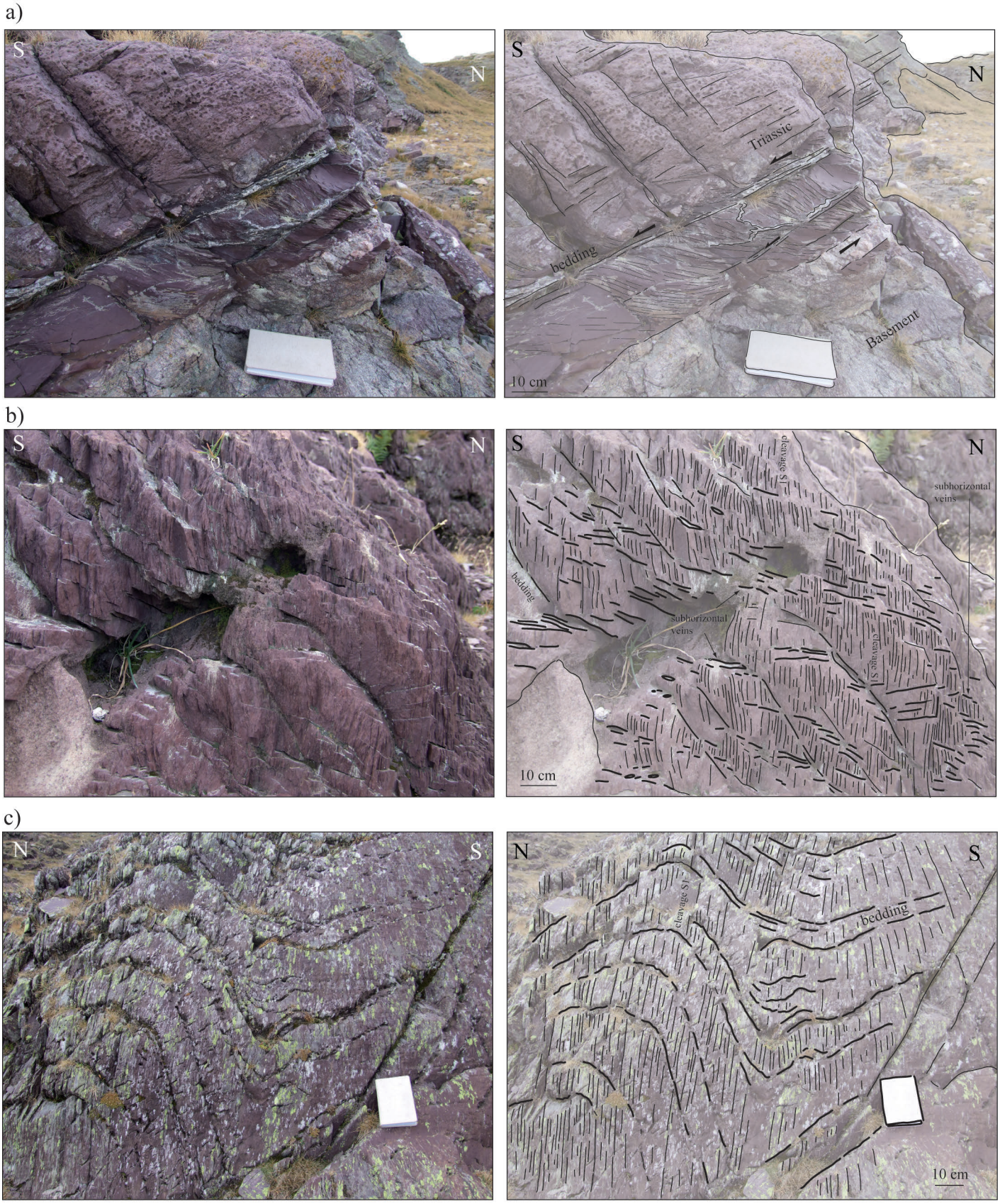
a)
S
N
S
N
Triassic
bedding
Basement
10 cm
b)
S
N
S
N
cleavage S1
subhorizontal veins
bedding
subhorizontal veins
cleavage S1
10 cm
c)
N
S
N
S
cleavage S1
bedding
10 cm

Figure 10

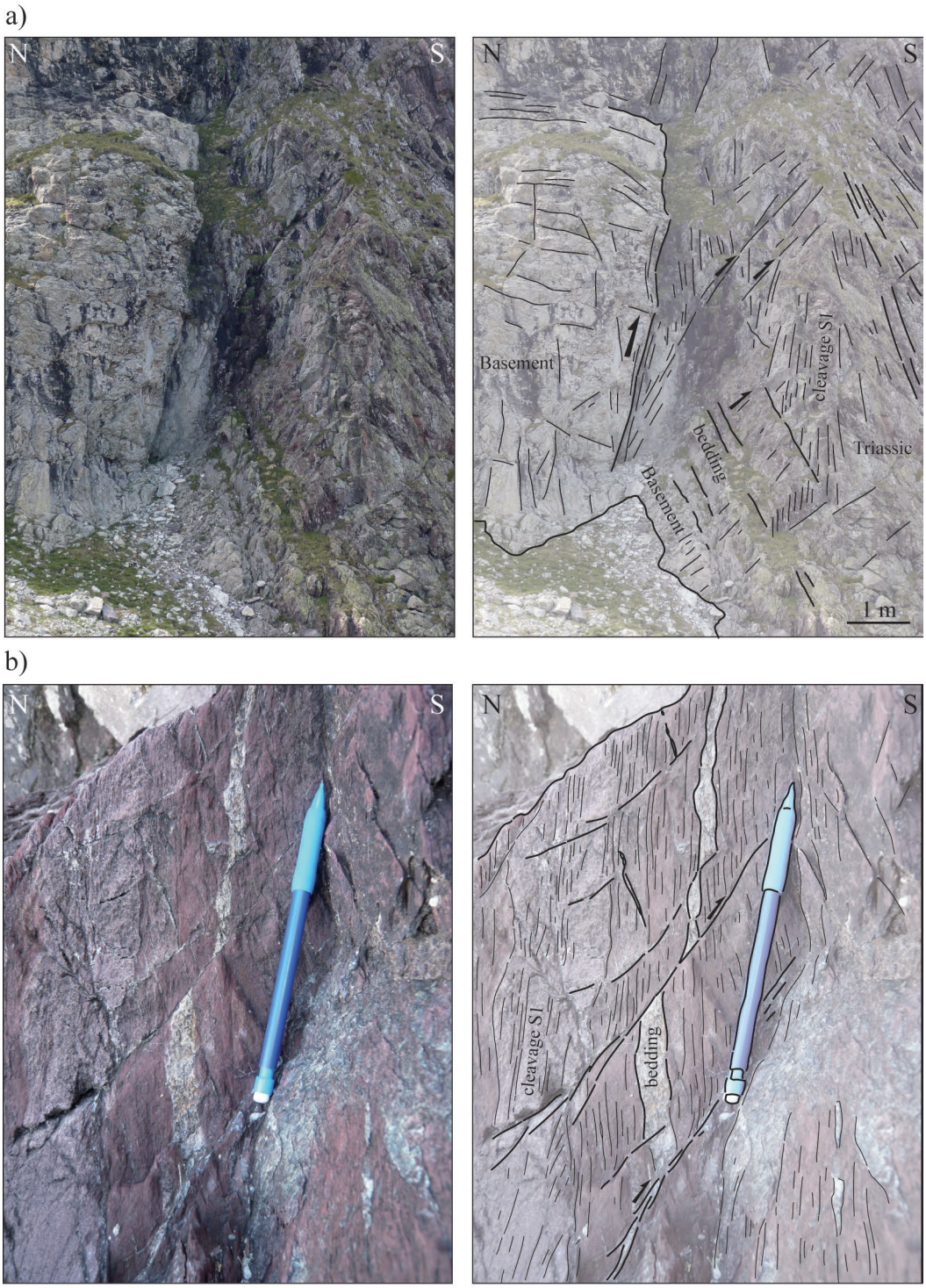
a)
N
S
N
S
Basement
cleavage S1
bedding
Triassic
Basement
1 m
b)
N
S
N
S
cleavage S1
bedding

Figure 11

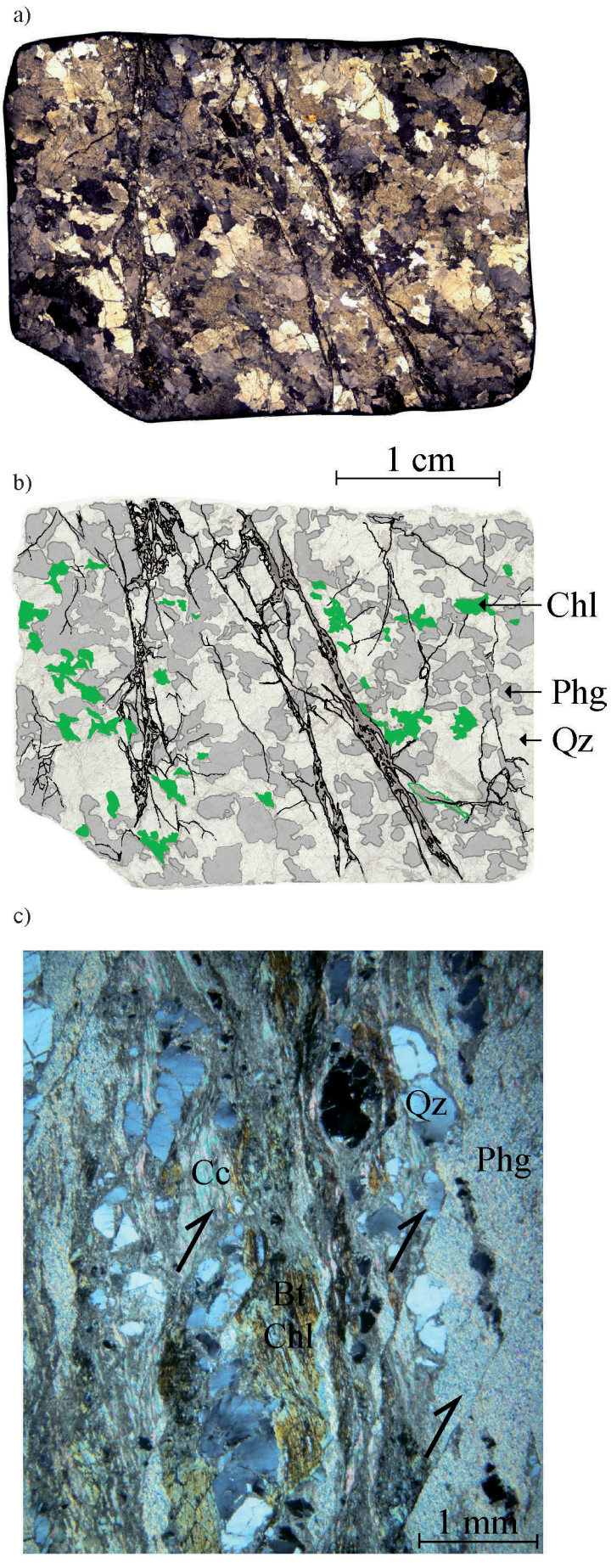

Figure 12

a)

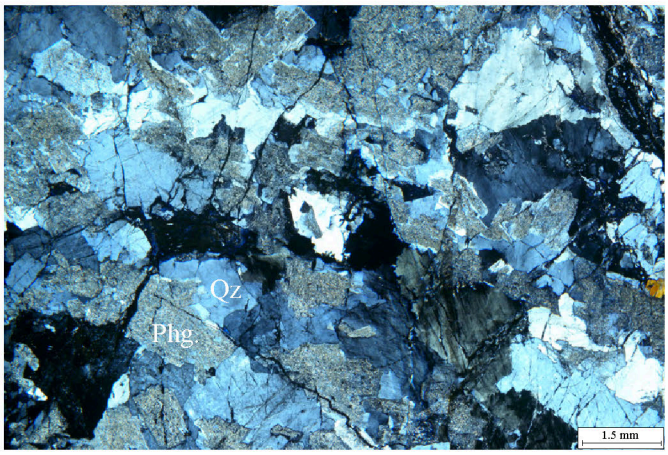

b)

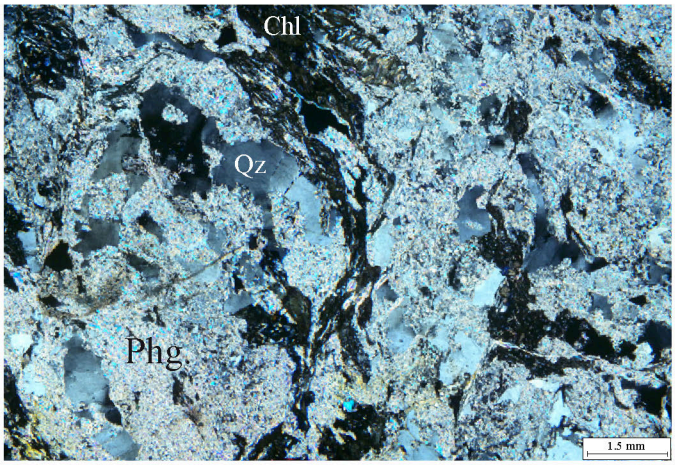

c)

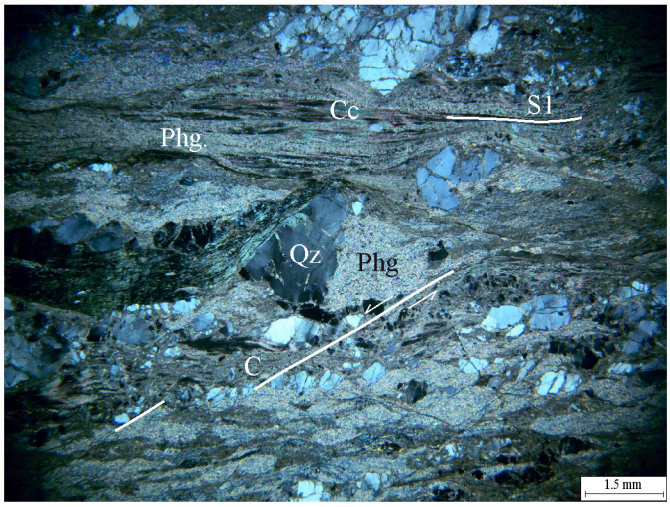

Figure 13

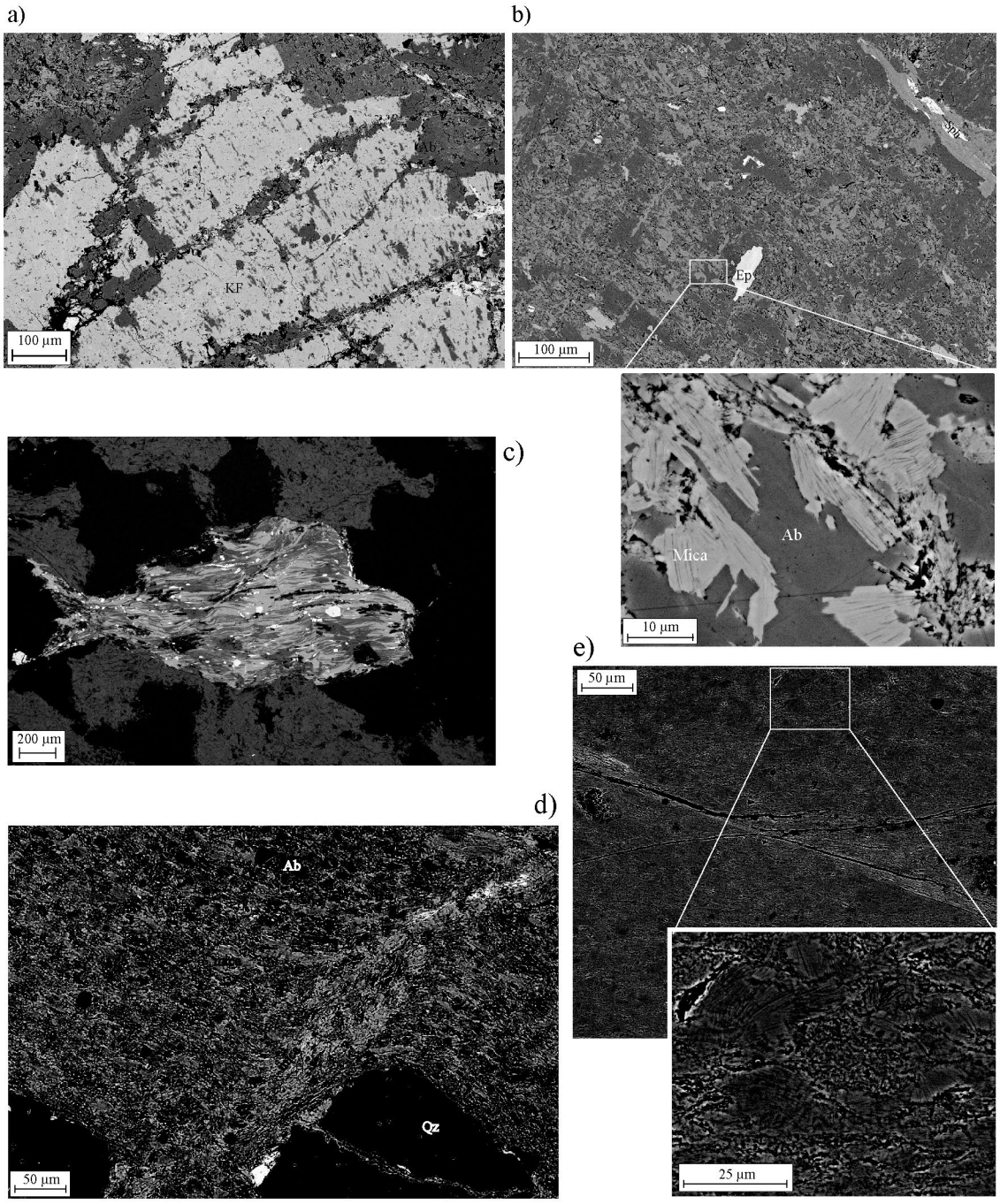
a)
b)
KF
Ab
Ep
Spl
100 µm
100 µm
c)
Ab
Mica
10 µm
200 µm
e)
50 µm
d)
Ab
Qz
50 µm
25 µm

Figure 14

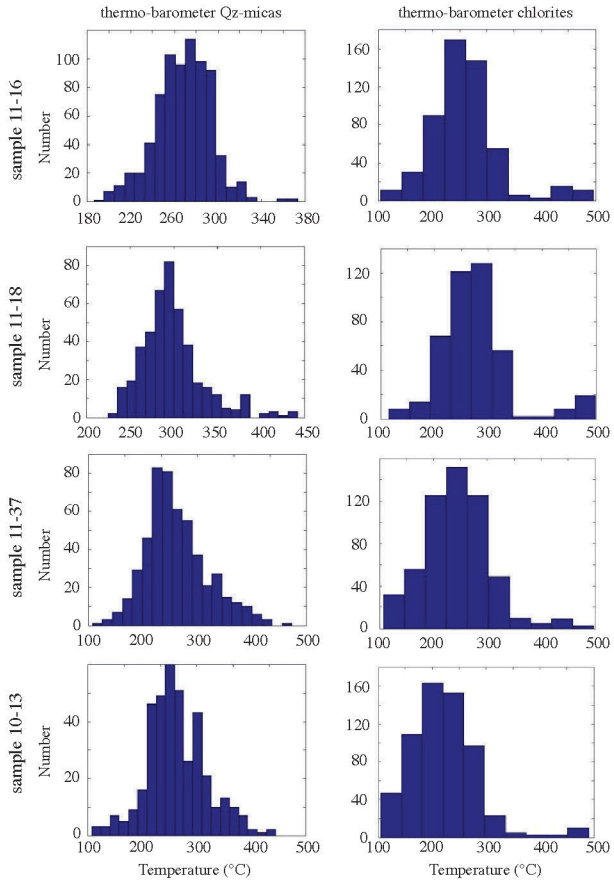
thermo-barometer Qz-micas
thermo-barometer chlorites
sample 11-16
sample 11-18
sample 11-37
sample 10-13
Number
Temperature (°C)

Figure 15

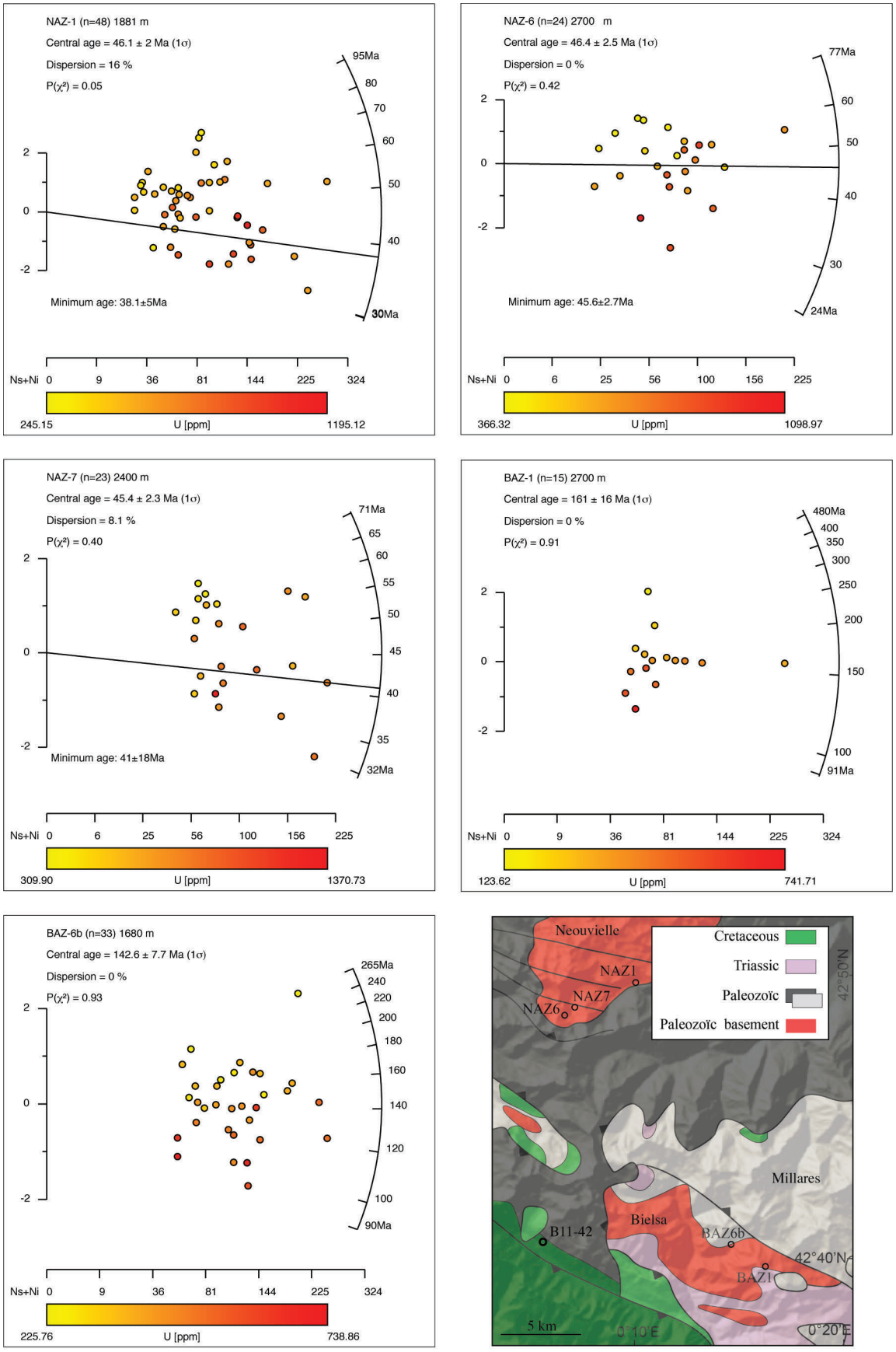
NAZ-1 (n=48) 1881 m
Central age = 46.1 ± 2 Ma (1σ)
Dispersion = 16 %
P(χ²) = 0.05
Minimum age: 38.1±5Ma
95Ma
80
70
60
50
40
30Ma
Ns+Ni 0 9 36 81 144 225 324
245.15 U [ppm] 1195.12
NAZ-6 (n=24) 2700 m
Central age = 46.4 ± 2.5 Ma (1σ)
Dispersion = 0 %
P(χ²) = 0.42
Minimum age: 45.6±2.7Ma
77Ma
60
50
40
30
24Ma
Ns+Ni 0 6 25 56 100 156 225
366.32 U [ppm] 1098.97
NAZ-7 (n=23) 2400 m
Central age = 45.4 ± 2.3 Ma (1σ)
Dispersion = 8.1 %
P(χ²) = 0.40
Minimum age: 41±18Ma
71Ma
65
60
55
50
45
40
35
32Ma
Ns+Ni 0 6 25 56 100 156 225
309.90 U [ppm] 1370.73
BAZ-1 (n=15) 2700 m
Central age = 161 ± 16 Ma (1σ)
Dispersion = 0 %
P(χ²) = 0.91
480Ma
400
350
300
250
200
150
100
91Ma
Ns+Ni 0 9 36 81 144 225 324
123.62 U [ppm] 741.71
BAZ-6b (n=33) 1680 m
Central age = 142.6 ± 7.7 Ma (1σ)
Dispersion = 0 %
P(χ²) = 0.93
265Ma
240
220
200
180
160
140
120
100
90Ma
Ns+Ni 0 9 36 81 144 225 324
225.76 U [ppm] 738.86
Neouvielle
NAZ1
NAZ7
NAZ6
Cretaceous
Triassic
Paleozoïc
Paleozoïc basement
42°50'N
Millares
Bielsa
B11-42
BAZ6b
BAZ1
42°40'N
5 km
0°10'E
0°20'E

Figure 16

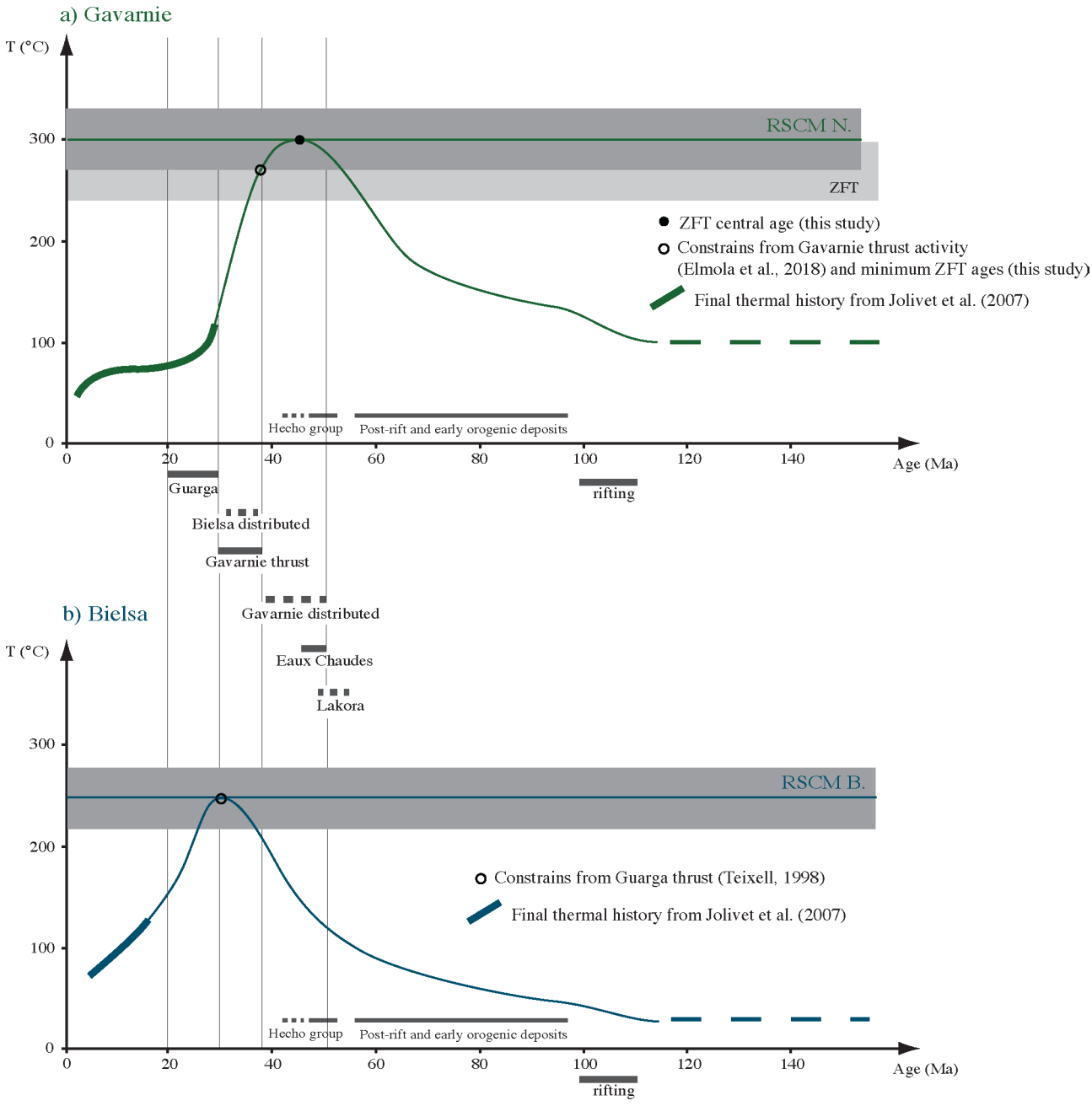
a) Gavarnie
T (°C)
300
200
100
0
RSCM N.
ZFT
ZFT central age (this study)
Constrains from Gavarnie thrust activity
(Elmola et al., 2018) and minimum ZFT ages (this study)
Final thermal history from Jolivet et al. (2007)
Hecho group
Post-rift and early orogenic deposits
0
20
40
60
80
100
120
140
Age (Ma)
Guarga
rifting
Bielsa distributed
Gavarnie thrust
Gavarnie distributed
b) Bielsa
Eaux Chaudes
Lakora
T (°C)
300
200
100
0
RSCM B.
Constrains from Guarga thrust (Teixell, 1998)
Final thermal history from Jolivet et al. (2007)
Hecho group
Post-rift and early orogenic deposits
0
20
40
60
80
100
120
140
Age (Ma)
rifting

Figure 17

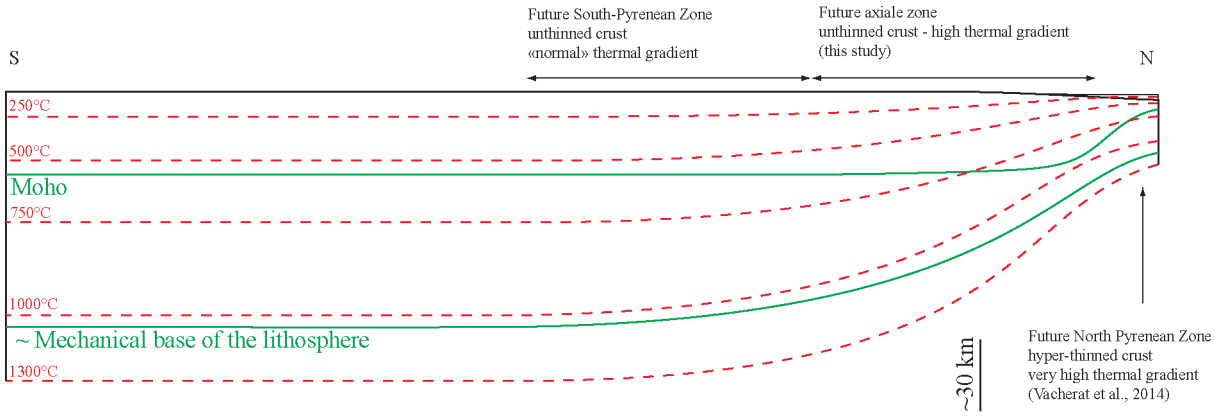
Future South-Pyrenean Zone
unthinned crust
«normal» thermal gradient
Future axiale zone
unthinned crust - high thermal gradient
(this study)
S
N
250°C
500°C
Moho
750°C
1000°C
~ Mechanical base of the lithosphere
1300°C
~30 km
Future North Pyrenean Zone
hyper-thinned crust
very high thermal gradient
(Vacherat et al., 2014)

Figure 18

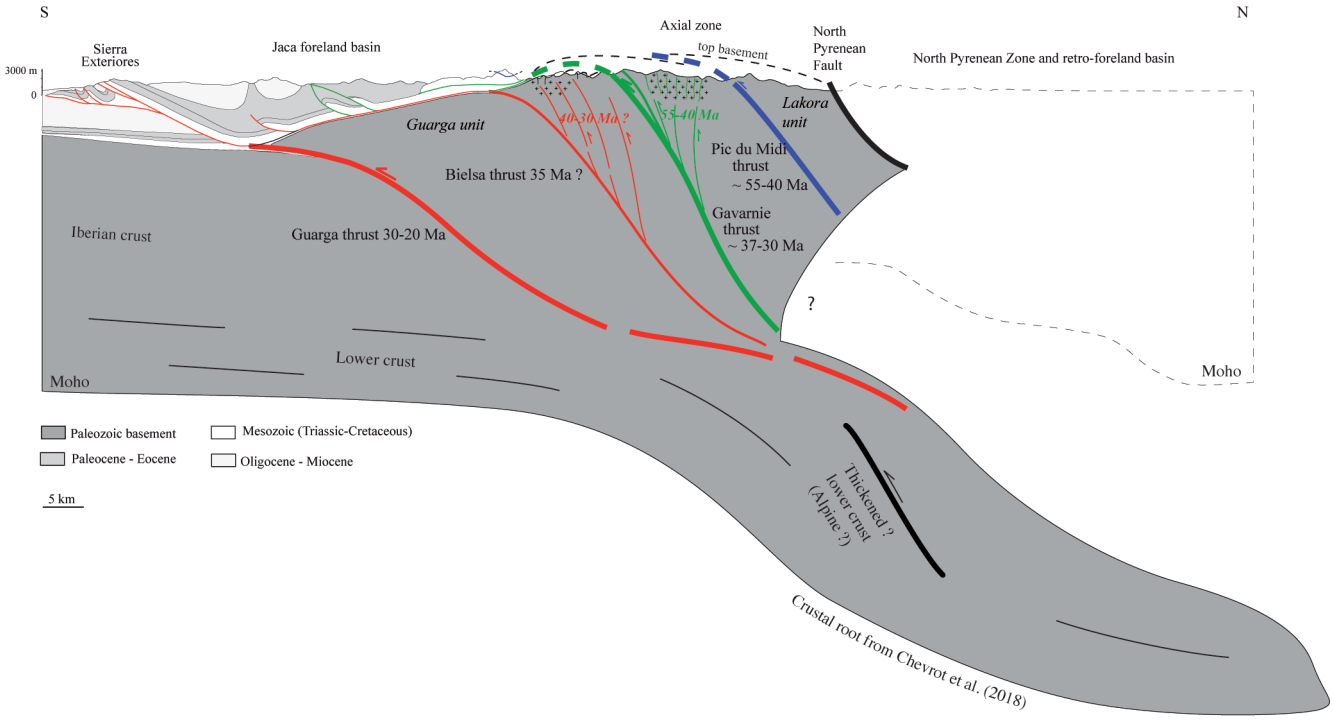
S
N
Sierra
Exteriores
Jaca foreland basin
Axial zone
top basement
North
Pyrenean
Fault
North Pyrenean Zone and retro-foreland basin
3000 m
0
Guarga unit
40-30 Ma ?
55-40 Ma
Lakora
unit
Pic du Midi
thrust
~ 55-40 Ma
Bielsa thrust 35 Ma ?
Gavarnie
thrust
~ 37-30 Ma
Iberian crust
Guarga thrust 30-20 Ma
?
Lower crust
Moho
Moho
Paleozoic basement
Paleocene - Eocene
Mesozoic (Triassic-Cretaceous)
Oligocene - Miocene
5 km
Thickened ? lower crust (Alpine ?)
Crustal root from Chevrot et al. (2018)

Figure 19

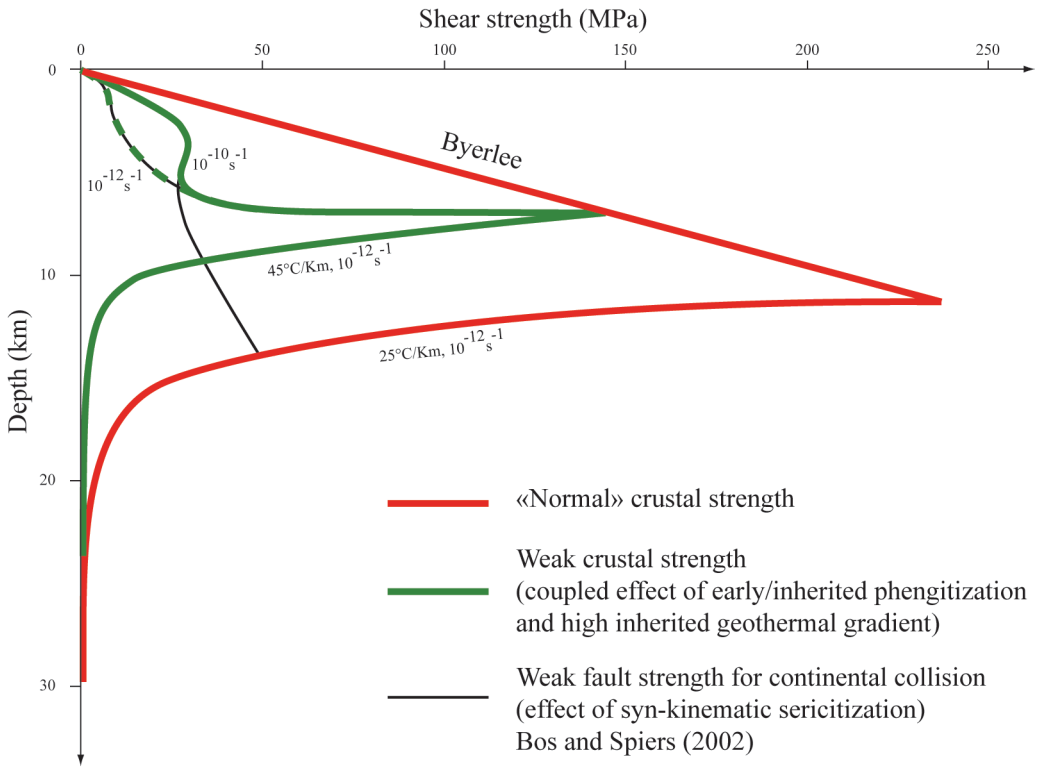
Shear strength (MPa)
0
50
100
150
200
250
0
10
20
30
Depth (km)
Byerlee
10-10 s-1
10-12 s-1
45°C/Km, 10-12 s-1
25°C/Km, 10-12 s-1
«Normal» crustal strength
Weak crustal strength
(coupled effect of early/inherited phengitization
and high inherited geothermal gradient)
Weak fault strength for continental collision
(effect of syn-kinematic sericitization)
Bos and Spiers (2002)

Figure 20

Sample	Raman parameter RA1 (Lahfid et al., 2010)		RSCM Temperature (°C)	
	Average	SD	average	SD
B11-9	0.60340626	0.016081064	264.0	19.6
B11-11	0.57516455	0.017642586	236.7	16.1
B11-42	0.65579392	0.005169598	327.8	6.3

Table 1: TMax obtained from RSCM method.

Sample n°	Elevation (m)	Rho-S x10^6 (Ns)	Rho-I x10^6 (Ni)	Rho-D x10^6 (Nd)	Grains	Dispersion %	P(X^2) %	Central age Ma	+/-	Minimum age Ma	+/-
BAZ-1	2528	12.6 (1161)	1.2 (111)	0.220 (3112)	15	0	91	161	16	155	16
BAZ-6B	1532	12.7 (3541)	1.37 (382)	0.220 (3114)	33	0	93	142.6	7.7	138.8	8.1
NAZ-1	1864	5.95 (3348)	2.03 (1142)	0.219 (3116)	48	16	5	46.1	2	38.1	5
NAZ-6	2707	6.3 (1406)	2.1 (469)	0.219 (3118)	24	0	42	46.4	2.5	45.6	2.7
NAZ-7	2423	7.2 (1718)	2.4 (587)	0.219 (3120)	23	8.1	40	45.4	2.3	41	18

Zeta value 141.69 +/- 4.66

Table 2. Zircon Fission Track dataset from Bielsa and Neouvielle plutonic massifs